Acta Biomaterialia xxx (xxxx) xxx

Contents lists available at ScienceDirect

Acta Biomaterialia

journal homepage: www.elsevier.com/locate/actbio

Full length article

Rapid specialization and stiffening of the primitive matrix in developing articular cartilage and meniscus

Bryan Kwok[a], Prashant Chandrasekaran[a], Chao Wang[a], Lan He[a], Robert L. Mauck[b,c], Nathaniel A. Dyment[b], Eiki Koyama[d], Lin Han[a,*]

[a] School of Biomedical Engineering, Science and Health Systems, Drexel University, Philadelphia, PA 19104, United States
[b] McKay Orthopaedic Research Laboratory, Department of Orthopaedic Surgery, Perelman School of Medicine, University of Pennsylvania, Philadelphia, PA 19104, United States
[c] Translational Musculoskeletal Research Center, Corporal Michael J. Crescenz Veterans Administration Medical Center, Philadelphia, PA 19104, United States
[d] Translational Research Program in Pediatric Orthopaedics, Division of Orthopaedic Surgery, The Children's Hospital of Philadelphia, Philadelphia, PA 19104, United States

ARTICLE INFO

Article history:
Received 20 February 2023
Revised 2 June 2023
Accepted 28 June 2023
Available online xxx

Keywords:
Embryonic development
Primitive matrix
Nanomechanics
Articular cartilage
Meniscus

ABSTRACT

Understanding early patterning events in the extracellular matrix (ECM) formation can provide a blueprint for regenerative strategies to better recapitulate the function of native tissues. Currently, there is little knowledge on the initial, incipient ECM of articular cartilage and meniscus, two load-bearing counterparts of the knee joint. This study elucidated distinctive traits of their developing ECMs by studying the composition and biomechanics of these two tissues in mice from mid-gestation (embryonic day 15.5) to neo-natal (post-natal day 7) stages. We show that articular cartilage initiates with the formation of a pericellular matrix (PCM)-like primitive matrix, followed by the separation into distinct PCM and territorial/interterritorial (T/IT)-ECM domains, and then, further expansion of the T/IT-ECM through maturity. In this process, the primitive matrix undergoes a rapid, exponential stiffening, with a daily modulus increase rate of 35.7% [31.9 39.6]% (mean [95% CI]). Meanwhile, the matrix becomes more heterogeneous in the spatial distribution of properties, with concurrent exponential increases in the standard deviation of micromodulus and the slope correlating local micromodulus with the distance from cell surface. In comparison to articular cartilage, the primitive matrix of meniscus also exhibits exponential stiffening and an increase in heterogeneity, albeit with a much slower daily stiffening rate of 19.8% [14.9 24.9]% and a delayed separation of PCM and T/IT-ECM. These contrasts underscore distinct development paths of hyaline versus fibrocartilage. Collectively, these findings provide new insights into how knee joint tissues form to better guide cell- and biomaterial-based repair of articular cartilage, meniscus and potentially other load-bearing cartilaginous tissues.

Statement of significance

Successful regeneration of articular cartilage and meniscus is challenged by incomplete knowledge of early events that drive the initial formation of the tissues' extracellular matrix in vivo. This study shows that articular cartilage initiates with a pericellular matrix (PCM)-like primitive matrix during embryonic development. This primitive matrix then separates into distinct PCM and territorial/interterritorial domains, undergoes an exponential daily stiffening of ≈36% and an increase in micromechanical heterogeneity. At this early stage, the meniscus primitive matrix shows differential molecular traits and exhibits a slower daily stiffening of ≈20%, underscoring distinct matrix development between these two tissues. Our findings thus establish a new blueprint to guide the design of regenerative strategies to recapitulate the key developmental steps in vivo.

* Corresponding author.
E-mail address: lh535@drexel.edu (L. Han).

https://doi.org/10.1016/j.actbio.2023.06.047
1742-7061/

1. Introduction

Regeneration of articular cartilage and meniscus is required to treat joint injury and slow osteoarthritis (OA) development, the most common musculoskeletal disease afflicting ≈ 15% of the adult population [1]. To date, however, regenerative products have not yet been able to effectively restore the functions of healthy, native tissues [2]. Articular cartilage and meniscus are two load-bearing tissues that interact directly with one another and are essential for knee joint function. Both tissues share a common cellular origin, arising from *Gdf5* (growth differentiation factor 5)-expressing progenitors in the interzone [3], a region of flattened, condensed mesenchymal cells at the prospective joint site in early development [4], and in sites flanking the interzone [5,6]. Despite this common origin, the extracellular matrices (ECMs) of these two tissues have distinct composition, structure and biomechanical properties in the adult. Articular cartilage ECM primarily consists of type II collagen fibrils and aggrecan-hyaluronan (HA) aggregates [7], while the meniscus ECM is dominated by circumferentially aligned type I collagen fibers, with a lower amount of collagen II and proteoglycans that are concentrated in the inner region [8]. Although efforts from the past several decades have yielded major advances in promoting the cellular biosynthesis of these primary ECM constituents in vitro in tissue engineered analogs, restoration of native tissue structural integrity and biomechanical functions remains a major challenge [2]. This is due, in part, to the fact that we do not yet fully understand how these unique native ECMs are established in vivo [9]. Understanding the initial events that drive ECM formation and development could provide a foundation to overcome this challenge [10].

We define the initial ECM in incipient embryonic tissues as the primitive matrix, which serves as the template that grows into the hierarchically structured, mechanically functional ECM upon maturation. This primitive matrix also establishes a microscale niche through which external biomechanical stimuli are transduced to resident cells, thereby mediating cell mechanosensitive activities. This renders the primitive matrix a crucial mediator of normal joint development, ensuring that the proper chemomechanical stimuli reach the cell to guide proliferation and differentiation. In articular chondrocytes, several mechanosensitive pathways are known to regulate embryonic development, including transforming growth factor-β (TGF-β) [11], Wnt/β-catenin [3], Ext1 [12], Hippo/Yap1 [13], β_1-integrin [14] and ion channel-mediated [15] signaling. Although meniscus development is less studied, some key pathways, such as TGF-β [16], bone morphogenetic protein (BMP) [17] and Hedgehog [18] signaling, have been shown to play major roles. For all joint tissues, the crucial role of biomechanical signaling is highlighted by impaired chondrogenesis and joint formation when these factors are reduced or removed during embryonic development in mouse, chicken and duck [19–23]. At the same time, previous studies have measured tissue-level biomechanical properties of fetal cartilage from various animals [24–27] and human donors [28,29], as well as fetal bovine meniscus [30]. At the microscale, atomic force microscopy (AFM)-based nanoindentation has been applied to quantify the micromodulus of fetal murine cartilage [31,32] and bovine meniscus [33]. Despite these efforts, a systematic understanding of the formation and development of the primitive matrices in these two tissues during this critical developmental phase has not been achieved.

To fill this knowledge gap, this study elucidated the time-evolving changes in the primitive matrix of articular cartilage and the meniscus during embryonic and early post-natal development. Using the wild-type (WT) murine model, we studied the morphology and sulfated glycosaminoglycan (sGAG) distribution of these primitive matrices within a well-defined time window. In murine knee joints, the initial deposition of structural ECM molecules takes place between embryonic day 14.5 (E14.5) and 15.5 (E15.5) [34]. We evaluated joints over a 14-day time window from the time of matrix initiation (E15.5) to post-natal day 7 (P7), during which, newborn pups were delivered at embryonic day 21.5, *i.e.*, P0 is equivalent to E21.5. In mature articular cartilage and meniscus, there exists a crucial microdomain that is in immediate contact with residing cells, termed the pericellular matrix (PCM) [35,36]. The PCM has a distinct composition and structure relative to the territorial/interterritorial domains that make up the bulk of the adult ECM (T/IT-ECM). Given its immediate contact with cells, the PCM plays a pivotal role in regulating cell-matrix mechanotransduction and disease initiation [37–39], and is the location where the initial assembly of collagen fibrils and aggrecan-HA aggregates occurs [40,41], with newly synthesized aggrecan molecules localized to the PCM in mature cartilage [42,43]. Because development of the PCM has not been studied, we assessed the formation of PCM versus T/IT-ECM at this early stage by evaluating the protein distribution and gene expression of collagen VI [44] and perlecan [45], the two biomarkers most commonly used for labeling the PCM [35,36]. We then quantified the local micromodulus of the primitive matrix within these domains by applying immunofluorescence (IF)-guided AFM nanomechanical mapping [38] and classical AFM nanoindentation [46]. The former enabled us to separate the properties of PCM versus T/IT-ECM, and to elucidate the time-evolving nanoscale mechanical heterogeneity in these regions. The latter enabled us to measure integrated mechanical properties of different tissue compartments, including the PCM, T/IT-ECM and regions corresponding to cell remnants. Additionally, to highlight the distinctive features of the primitive matrix in articular cartilage, we also included epiphyseal cartilage in the analysis of matrix composition and classical AFM nanoindentation. Epiphyseal cartilage is another hyaline cartilage tissue dominated by collagen II and aggrecan. During joint development, however, unlike articular cartilage, epiphyseal cartilage remodels into subchondral bone, rather than staying permanently as hyaline cartilage [47]. Collectively, outcomes from this work highlight a rapid specialization and stiffening of the primitive matrices in both articular cartilage and the meniscus, and define the distinct characteristics of the initial matrix templates that give rise to hyaline cartilage and fibrocartilage.

2. Methods

2.1. Histology and immunofluorescence imaging

Knee joints were harvested from wild-type (WT) C57BL/6J mice (Jackson Laboratory) at 15.5 and 17.5 days after fertilization (E15.5 and E17.5, from pregnant dams), at birth (P0) and at post-natal day 7 (P7). To ensure consistency, only pups delivered at embryonic day 21.5 (E21.5) were included for post-natal time points P0 and P7 studies. Animal sex was not delineated at these early developmental time points. All animal work was approved by the Institutional Animal Care and Use Committee (IACUC) at Drexel University. Whole joints were fixed in 4% paraformaldehyde, embedded in paraffin, and sectioned into serial 5 μm-thick sagittal sections ($n = 4$ animals/time point). Histology and immunofluorescence (IF) imaging was performed on these sections to analyze the composition and morphology of articular cartilage, epiphyseal cartilage and the meniscus. To assess cellularity and sGAG distribution, Hematoxylin and Eosin (H&E) and Safranin-O/Fast Green histology staining were applied. To assess the distributions of cartilage PCM biomarkers, sections were incubated with the primary antibodies in 1% bovine serum albumin (BSA), 1 × PBS for collagen VI (70R-CR009X, Fitzgerald, 1:100 dilution, with specificity authenticated in [48]) and perlecan (A7L6-MA1-06821, Invitrogen, 1:100) overnight in 4°C, following the established procedure [38]. Sections

were then incubated with corresponding secondary antibodies for collagen VI (A11008, Invitrogen, 1:200) and perlecan (112-156-003, Jackson ImmunoResearch, 1:200), respectively, for 1 hour at room temperature and finally counterstained with DAPI Fluoromount-G (0100-20, SouthernBiotech). For all the staining, internal negative controls were prepared following the same procedures but without the incubation of primary antibodies. For histology, brightfield images were taken using a Leica DM4000 B microscope (Leica Microsystems). For IF imaging, fluorescence images were taken using a Leica DMI-6000B microscope with a 488 nm and a 555 nm fluorescent lamp at 50% power and 300 ms exposure time in a 16-bit, 1,392 × 1,040 imaging array format.

The IF images of collagen VI were analyzed to quantify the area proportions of cell, PCM and T/IT-ECM domains in articular cartilage, using the *Trainable Weka Segmentation* algorithm in ImageJ [49], as a surrogate for their volume proportions in 3D. In brief, the areas corresponding to cell, PCM and T/IT-ECM within each region of interest (ROI) were defined by the distribution of collagen VI [38] to train the machine learning algorithm to classify entire image regions of articular cartilage (≥ 3-5 images each animal, $n = 4$/time point). Following the classification, images were further processed to remove the background noise using the *thresholding* function and converted to binary format. The area proportion for each domain within each ROI was then calculated using the *analyze particles* function. To detail articular cartilage matrix development from inception to maturity, we performed our analysis on collagen VI IF images from this study and those from our previous analysis at post-natal ages P3, P14 and P90 [50].

2.2. RNAscope fluorescent in situ hybridization

To assess the spatial gene expression patterns of collagen VI, perlecan and aggrecan, RNAscope fluorescent in situ hybridization was performed to visualize the spatiotemporal expressions of *Col6a1, Hspg2* and *Acan* genes, following the established procedure [51]. In brief, RNAscope was carried out using RNAscope Multiplex Fluorescent v2 (Advanced Cell Diagnostics, or ACD) to visualize the expressions of collagen VI $\alpha 1$ chain (*Col6a1*, 443261, ACD), perlecan (*Hspg2*, 493051-C2, ACD) and aggrecan (*Acan*, 439101, ACD) in murine knee joints at the ages of E15.5, E17.5, P0 and P7 ($n = 4$/time point). Knee paraffin sections were pre-treated with a custom reagent (300040, ACD) and hybridized with each probe for 2 hours at 40°C in a custom oven. Signal was amplified with pre-amplifier and multiple amplifier as per manufacturer's protocols. Negative control probes (320871, ACD) were used to ensure signal specificity. Sections were counterstained with Hoechst 33342 (H21492, Invitrogen) and sealed with ProLong Gold Antifade Mount (36930, Invitrogen).

2.3. Immunofluorescence (IF)-guided AFM nanomechanical mapping

To quantify the biomechanics of developing primitive matrix, we applied IF-guided AFM nanomechanical mapping on unfixed sagittal cryo-sections of the knee joint, following our established procedure [38]. Freshly dissected knee joints were harvested from WT mice, embedded in optimal cutting temperature (OCT) media, and cryo-sectioned into 8 μm-thick, unfixed sagittal sections via the Kawamoto's film-assisted method [52]. The sections were fluorescently labeled for collagen VI, following the established procedure [38]. In brief, the sections were washed with 1 × PBS to remove OCT, blocked with 10% goat serum for 20 min at room temperature, and then, incubated with collagen VI primary antibody (70R-CR009X, Fitzgerald, 1:100 dilution) for 20 min, washed twice with 1 × PBS for 5 min each, and finally, incubated with the secondary antibody (A11008, Invitrogen, 1:200) for 20 min in darkness. This labeling procedure has been validated not to alter the micromechanical properties of the samples [38,53]. Immediately following the labeling, sections were tested using the Total Internal Reflection Fluorescence (TIRF)-AFM (MFP-3D, Asylum Research) in 1 × PBS with protease inhibitors (Pierce 88266, ThermoFisher). We performed the AFM nanomechanical mapping on sections from E17.5, P0 and P7 joints ($n = 5$/time point). We did not include samples from E15.5 for this test, because the weak fluorescent signal of collagen VI at this earlier time point prevented us from discerning the matrix versus cells.

On each section, within each region corresponding to articular cartilage and outer zone of the meniscus, we identified three to five 20 × 20 μm^2 regions of interest (ROIs) with well-defined, collagen VI-positive PCM terrains. The nanomechanical mapping was performed in a 40 × 40 grid (1,600 indentations) within each ROI using polystyrene microspherical tips ($R \approx 2.25$ μm, nominal $k \approx 0.6$ N/m, HQ:NSC36/tipless/Cr-Au, cantilever C, NanoAndMore) up to a maximum indentation depth of $d_{max} \approx 100$ nm at 10 μm/s z-piezo displacement rate (corresponding to ≈ 0.01 sec loading time). On each section, each ROI was at least 40 μm apart to avoid overlapping, and the maximum indentation depth was within the limit of small indentation regime, $d_{max} < 0.2H$ (thickness of the cryo-section) [54], and Hertzian contact framework, $d_{max} < 0.2R$ [55]. The effective indentation modulus, E_{ind}, was calculated by fitting the entire loading portion of the indentation force-depth (F-D) curve to the finite thickness-corrected Hertz Model [56], assuming the Poisson's ratio, $\nu = 0.1$ for cartilage [57] and 0 for the meniscus [58]. The choice of Poisson's ratios here was based on values reported for bovine cartilage [57] and meniscus [58], and may not accurately represent the values for developing murine tissues. However, according to the Hertz model, we expect the values of Poisson's ratio to have minimal impact on the quantitative modulus outcomes. For example, varying ν from 0 to 0.1 only yielded ≈ 1% difference in E_{ind}, and was not expected to influence major conclusions of this study. Next, using the corresponding IF images of collagen VI, we separated the E_{ind} of PCM and T/IT-ECM using a custom MATLAB (Mathworks) program when applicable, and excluded values corresponding to cell remnants (*e.g.*, cellular debris consisting of cytoplasmic organelles and nucleus damaged during sectioning) [38].

2.4. Classical AFM nanoindentation

To test if tissue stiffening takes place at a larger length scale integrating the primitive matrix and cells, and if the stiffening starts as soon as the inception of primitive matrices at E15.5, classical AFM nanoindentation was applied to the same OCT-embedded, 8 μm-thick sagittal cryo-sections at all four ages from E15.5 to P7 ($n = 5$ animals/group), following the established procedure [59,60]. On each section, AFM nanoindentation was performed in 1 × PBS with protease inhibitors using polystyrene microspherical tips ($R \approx 12.45$ μm, nominal $k \approx 0.6$ N/m, HQ:NSC36/tipless/Cr-Au, cantilever C, NanoAndMore) and a Dimension Icon AFM (Bruker Nano). For each sample, within each region corresponding to articular cartilage, epiphyseal cartilage and meniscus, at least 15 different indentation locations were randomly chosen and tested up to a maximum indentation depth of $d_{max} \approx 1$ μm at 10 μm/s rate (corresponding to ≈ 0.1 sec loading time). Inclusion of epiphyseal cartilage here allowed us to assess differences in the initial development of articular versus epiphyseal cartilage. Similar to the case of IF-AFM nanomechanical mapping, the maximum indentation depth was also within the limit of small indentation regime, *e.g.,* $d_{max} < 0.2H$ (thickness of the cryo-section) [54] and Hertzian contact framework, *e.g.,* $d_{max} < 0.2R$ [55]. Thus, the effective indentation modulus, E_{ind}, was calculated from the finite thickness-corrected Hertz model [56], assuming $\nu = 0.1$ for articular and epiphyseal cartilage [57], and 0 for the meniscus [58].

2.5. Analysis of age-dependent evolvement in matrix micromodulus and spatial heterogeneity

In classical AFM nanoindentation, the use of a larger microspherical indenter, $R \approx 12.45$ µm, with a ≈ 1 µm maximum indentation depth resulted in a tip-sample contact radius of ≈ 4.9 µm, suggesting that the modulus outcomes represent integrated indentation responses of both the matrix and cell remnants. We therefore denote the indentation modulus measured from this modality as E_{Tissue} (in Pa). In contrast, in IF-AFM nanomechanical mapping, a smaller microspherical indenter, $R \approx 2.25$ µm, was used to apply ≈ 100 nm maximum indentation depth, resulting in $\approx$ 0.7 µm contact radius. For nanoindentation with spherical indenters, the stress fields are largely constrained to the region directly underneath the tip-sample contact area within the Hertzian contact framework [61,62]. The use of the smaller indenter ($R \approx 2.25$ µm) thus yielded a spatial resolution at the sub-µm level, much smaller than the size of a cell ($\approx$ 10-30 µm in diameter [63]) or thickness of the PCM ($\approx$ 2-4 µm in thickness [37,64,65]). Therefore, we separated the micromodulus of the primitive matrix from those corresponding to cell remnants, and denoted the modulus values as E_{Matrix} (in Pa). In addition, when distinct PCM and T/IT-ECM compartments could be identified at later ages, guided by the IF-labeling of collagen VI again, we separated the values of the two domains, E_{PCM} and $E_{\text{T/IT-ECM}}$, respectively, for further analysis of micromechanical heterogeneity (Table 1).

To elucidate the age-dependent stiffening of the primitive matrix, the average modulus was calculated from each animal and tissue type at each age. For IF-guided AFM nanomechanical mapping, average modulus was calculated combined for the entire primitive matrix, and separately for PCM versus T/IT-ECM. For classical AFM nanoindentation, the average modulus was calculated for the entire tissue. For each tissue, simple least-squares linear regression was applied to the logarithmic transform of averaged E_{ind} (in Pa), $log_{10}(E_{\text{ind}})$, with respect to age (in days, $t = 0$ at E15.5, and $t = 6$ at P0) for the primitive matrix modulus, E_{Matrix}, and the PCM-only modulus, E_{PCM} (for articular cartilage), measured from IF-AFM nanomechanical mapping, as well as the integrated tissue modulus, E_{Tissue}, measured from classical AFM nanoindentation. For articular cartilage, to detail the evolvement of E_{Matrix} and E_{PCM} from inception to maturity, we integrated results from this study with our previous analysis of murine articular cartilage at post-natal ages P3, P14 and P90 using the same procedures [50].

To assess the age-dependent evolvement of matrix spatial heterogeneity, we measured the absolute and relative variability of E_{Matrix}, as well as its correlation with the corresponding Euclidean distance to cell surface. For each modulus map, the standard deviation, s_E, was directly calculated from the modulus values corresponding to the matrix, E_{Matrix}, and the coefficient of variation, or relative standard deviation, s_{ER}, was calculated as the ratio of standard deviation over the average of E_{Matrix}. Least-squares linear regression was applied to estimate the slope β_s between $log_{10}(s_E)$ versus age, t in days (Table 2), as a measure of the longitudinal changes in matrix heterogeneity.

In addition, for each location, the matrix-to-cell Euclidean distance, $d_{\text{Matrix-to-Cell}}$, values were calculated as the closest distance of each matrix location to cell surface via the *bwdist* function in MATLAB (MathWorks). For matrix locations near the edge of each ROI, there could be an over-estimation of $d_{\text{Matrix-to-Cell}}$ since the cells closer to the location may not be included in the map. To minimize such systematic bias, for each ROI, we further identified a region defined by lines connecting the center of individual cell domains in the map, and only matrix locations within the region were included in the analysis. For each map, least-squares linear regression was applied to estimate the slope, b_d, between E_{Matrix} and $d_{\text{Matrix-to-Cell}}$, as a measure of matrix heterogeneity. Next, the average of b_d was calculated for each animal measured on articular cartilage and meniscus at each age. Least-squares linear regression was then applied to estimate the slope, β_d, between $log_{10}(b_d)$ versus age, t, in days (Table 2), as the second measure of the longitudinal changes in matrix heterogeneity.

Table 1
Glossary of quantitative experimental parameters and outcomes.

Parameters	Unit	Definition
t	day	animal age, $t = 0$ at E15.5, and $t = 6$ at P0 (equivalent to E21.5)
E_{Tissue}	Pa	micromodulus of the tissue (integrating regions of both matrix and cell remnants), as measured by classical AFM nanoindentation (indenter tip $R \approx$ 12.45 µm)
E_{Matrix}	Pa	micromodulus of the primitive matrix (including both PCM and T/IT-ECM), as measured by IF-AFM nanomechanical mapping (indenter tip $R \approx 2.25$ µm)
E_{PCM}	Pa	micromodulus of the pericellular matrix (PCM), as measured by IF-AFM nanomechanical mapping (indenter tip $R \approx 2.25$ µm)
$E_{\text{T/IT-ECM}}$	Pa	micromodulus of the territorial/interterritorial matrix (T/IT-ECM), as measured by IF-AFM nanomechanical mapping (indenter tip $R \approx 2.25$ µm)
s_E	Pa	absolute standard deviation, of E_{Matrix} within each region of interest
s_{ER}		coefficient of variation, or relative standard deviation, of E_{Matrix} within each region of interest
$d_{\text{Matrix-to-Cell}}$	µm	Euclidean distance of matrix to cell surface within each region of interest

2.6. Statistical analysis

To test the age-dependence of area percentages of cell, PCM and T/IT-ECM, following the confirmation of data normality via Shapiro-Wilk test [66] and heteroscedasticity via Bartlett's test [67], Welch's ANOVA [68] was applied, followed by the Games-Howell multiple comparison [69]. The linear mixed model was applied to test the significance of E_{Tissue}, E_{Matrix}, s_E, s_{ER}, and b_d using the R package lme4 (version1.1-29) [70]. In these tests, age, tissue type and matrix region (PCM versus T/IT-ECM) were treated as fixed effect factors when appropriate, and individual animal was treated as a random effect factor, with interaction terms between age and tissue type. Likelihood ratio test was applied to determine the choice of two covariance structures, unstructured versus compound symmetry. To account for the exponential increase in modulus and its variance with age, logarithmic transformation was applied to E_{Tissue}, E_{Matrix}, s_E and b_d. For log-linear regression outcomes, following the confirmation of data heteroscedasticity via Bartlett's test, Welch's ANOVA [68] was applied to compare α_E and β_E from classical AFM nanoindentation amongst the three tissue types, followed by Games-Howell multiple comparison [69]. Unpaired two-sample student's t-test was applied to compare α_E, β_E, β_s and β_d from IF-AFM nanomechanical mapping between articular cartilage and the meniscus, and to compare α_E and β_E between the two AFM modalities for each tissue, followed by Holm-Bonferroni multiple contrast correction [71]. One-way ANOVA was applied to compare amongst the daily increasing rates β_E, β_s and β_d for articular cartilage, followed by Tukey-Kramer multiple comparison and Welch's ANOVA was applied for the meniscus, followed by Games-Howell multiple comparison [69]. In all the tests, the significance level was set at $\alpha = 0.05$.

Table 2
Glossary of linear and log-linear regression analysis parameters.

Parameters	Unit	Definition
1) Exponential increase of modulus, E_{Matrix} or E_{Tissue}, with animal age: $log_{10}(E) = log_{10}(\alpha_E) + log_{10}(\beta_E) \cdot t$, or $E = \alpha_E \cdot \beta_E{}^{t}$		
α_E	Pa	initial value of modulus at $t = 0$
β_E	–	base of the exponential increase of modulus with age
2) Exponential increase of matrix modulus standard deviation, s_E, with animal age: $log_{10}(s_E) = log_{10}(\alpha_s) + log_{10}(\beta_s) \cdot t$, or $s_E = \alpha_s \cdot \beta_s{}^{t}$		
α_s	Pa	initial value of modulus standard deviation, s_E at $t = 0$
β_s	–	base of the exponential increase of s_E with age
3) Dependence of E_{Matrix} on $d_{\text{Matrix-to-Cell}}$: $E_{\text{Matrix}} = a_d + b_d \cdot d_{\text{Matrix-to-Cell}}$		
a_d	Pa	intercept of the extrapolated modulus at $d_{\text{Matrix-to-Cell}} = 0$
b_d	Pa·μm^{-1}	slope of the modulus increase with distance to cell surface, $d_{\text{Matrix-to-Cell}}$
4) Exponential increase of the slope, b_d, with animal age: $log_{10}(b_d) = log_{10}(\alpha_d) + log_{10}(\beta_d) \cdot t$, or $b_d = \alpha_d \cdot \beta_d{}^{t}$		
α_d	Pa·μm^{-1}	initial value of the slope, b_d, at $t = 0$
β_d	–	base of the exponential increase of b_d with age

3. Results

3.1. Separation of the PCM and T/IT-ECM in the primitive matrix of articular cartilage

From E15.5 to P7, the knee joint increased in size, organization and matrix deposition (Fig. 1a). The increased staining of sGAGs (red) illustrated the deposition of aggrecan, the major proteoglycan in cartilage [7]. Analyzing the spatial distributions of PCM biomarkers at E15.5, we noted only weak signal for collagen VI and no signal for perlecan in articular cartilage (Fig. 1b). At E17.5, both molecules became ubiquitously distributed throughout the intercellular spacing. This ubiquitous presence of collagen VI was consistent with literature on its distribution pattern in murine humeral head articular cartilage at E12.5 [72], as well as knee cartilage of newborn gray short-tailed opossum at P1 [73]. At P0, these two molecules were localized within ring-like microdomains surrounding each chondrocyte, illustrating a clear separation of PCM and T/IT-ECM at this time point. At P7, the PCM domains were further separated with the expansion of T/IT-ECM (Figs. 1b, 2a). Analyzing the longitudinal changes in the area proportions of PCM, T/IT-ECM and cells, we found a gradual decrease in the area percentage occupied by cells, from 84.4 ± 7.3% at E15.5 (mean ± 95% CI, $n = 4$) to 27.9 ± 6.8% at P7, and to 20.0 ± 1.5% at P90 (Fig. 2b). Over the same time window, the area of PCM first increased from 15.6 ± 7.3% at E15.5 to 38.5 ± 1.6% at P7, but then decreased to 28.5 ± 1.5% at P14 and 21.1 ± 1.1% at P90. This decrease was concurrent with a progressive increase in the area of T/IT-ECM from P0 (9.7 ± 3.1%) to P90 (58.9 ± 1.3%). Collectively, these data showed that articular cartilage initiated with a PCM-like primitive matrix characterized by the ubiquitous presence of collagen VI and perlecan (Figs. 1b, 2a). This was followed by the separation of distinct PCM and T/IT-ECM domains, and then, expansion of the T/IT-ECM until such point that it represented the bulk of the matrix at maturity.

3.2. Distinct composition of the primitive matrices in cartilage versus meniscus

Next, we highlighted differences in the primitive matrix compositions of hyaline cartilage versus fibrocartilage by analyzing the distributions of collagen VI and perlecan in articular cartilage, epiphyseal cartilage and the meniscus. We found that, as soon as they were individually distinguishable, the primitive matrices of these three units already showed distinct molecular signatures. At E17.5, in contrast to the strong presence of both collagen VI and perlecan in articular cartilage, the meniscus matrix showed much weaker staining for perlecan (Figs. 1b, 2c). Meanwhile, the epiphyseal cartilage matrix had no staining for collagen VI (Figs. 1b, 2a), similar to the localization pattern of collagen VI in the prospective joint sites of the embryonic humerus [72]. At P0, for both articular and epiphyseal cartilage, separation of PCM and T/IT-ECM was clearly evident by the localization of perlecan and/or collagen VI. In contrast, for the meniscus, collagen VI continued to be distributed throughout the matrix at P0, and only started to show localization into pericellular domains at P7 (Fig. 2c). Thus, the delineation between PCM and T/IT-ECM domains in the meniscus was delayed relative to that of articular and epiphyseal cartilage.

3.3. Differential gene expression profiles of matrix molecules in cartilage versus meniscus

We then validated the protein distributions of collagen VI and perlecan by assessing their spatial gene expression patterns via RNAscope fluorescent in situ hybridization. From E15.5 to P7, *Col6a1* was highly expressed in articular cartilage and meniscus cells, but absent in the hypertrophic chondrocytes of epiphyseal cartilage (Fig. 3a). The perlecan gene, *Hspg2*, had low expression in the joint at E15.5, but was upregulated in both articular and epiphyseal cartilage starting at E17.5 (Fig. 3b). These patterns confirmed the differential protein distributions amongst these tissues (Figs. 1b, 2a, 2c). We also assessed the expression of the major proteoglycan, aggrecan, and found high *Acan* expression in all three tissues (Fig. 3c), illustrating active cell biosynthesis activities. At this stage, *Acan* expression was lower in articular cartilage relative to epiphyseal cartilage, consistent with the contrast in the staining intensity of sGAGs (Fig. 1a). We also noticed some differences in the gene expression versus protein staining distributions. For example, the expression of *Col6a1* in articular cartilage was high at E15.5, but reduced at later ages (Fig. 3a). However, there was high level of collagen VI protein staining throughout all tested ages. This may indicate that collagen VI production possibly takes place at an early development phase, which then, undergoes slow turnover following its biosynthesis. Also, we found active expressions of *Hspg2* and *Acan* genes in meniscus cells, but the level of protein staining was low (Figs. 1, 2c). One possible explanation is that the

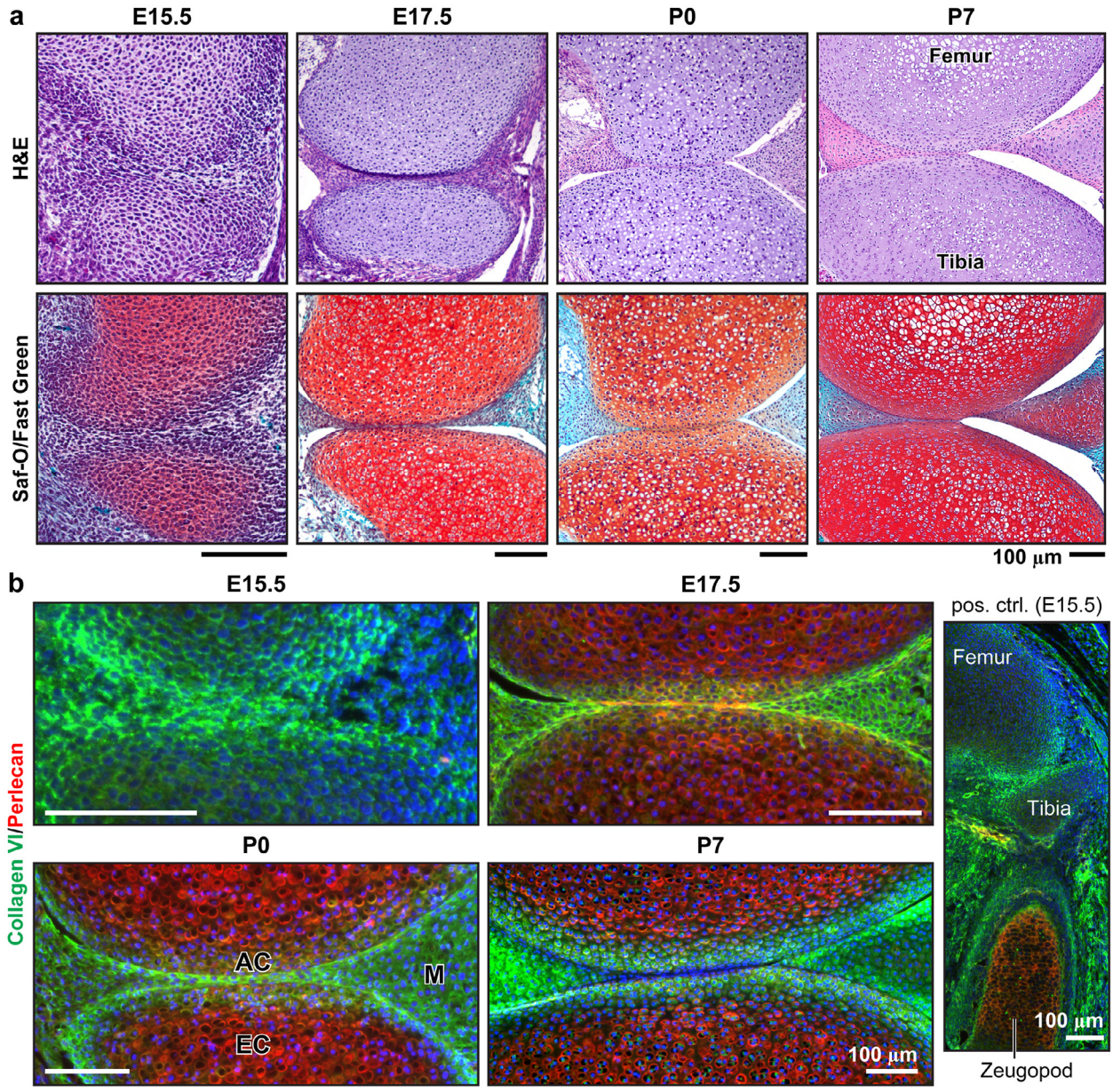

Fig. 1. Joint morphology and distribution of pericellular matrix (PCM) molecules in the developing murine knees at embryonic day 15.5 and 17.5 (E15.5 and E17.5), and at post-natal day 0 and 7 (P0 and P7). a) Representative Hematoxylin and Eosin (H&E) and Safranin-O/Fast Green (Saf-O/Fast Green) histology images show increased size, organization, as well as the deposition of sulfated glycosaminoglycans (sGAGs) during development. b) Immunofluorescence (IF) images of PCM biomarkers show that collagen VI (green) is present in articular cartilage (AC) and the meniscus (M), but not in epiphyseal cartilage (EC), while perlecan (red) is present in articular and epiphyseal cartilage, but not in the meniscus ($n = 4$, blue: DAPI). Internal positive control is shown in the right panel inset: positive staining of perlecan in the zeugopod at E15.5.

transcriptional gene expression may not have translated to protein biosynthesis in meniscus cells yet. Nevertheless, the spatial variations of these key matrix genes highlighted differential cell biosynthesis activities amongst these three tissues, which contribute to the distinct composition of their primitive matrices.

3.4. Rapid stiffening of the articular cartilage primitive matrix

Applying IF-guided AFM nanomechanical mapping, we detected a rapid stiffening of the articular cartilage primitive matrix. The micromodulus, $E_{\text{Matrix, AC}}$, increased from 8.44 ± 1.60 kPa at E17.5 (mean ± 95% CI, $n = 5$) to 38.8 ± 14.2 kPa at P0 (4.6 ± 0.5-fold, mean ± 95% CI) and 251 ± 49 kPa at P7 (29.8 ± 2.7-fold, Fig. 4a,b). Integrating these results with the micromodulus of articular cartilage matrix measured at P3, P14 and P90 in our previous study using the same method [50], we found a log-linear dependence of $E_{\text{Matrix, AC}}$ on animal age, from E17.5 to P7,

$$log_{10}\left(E_{\text{Matrix, AC}}\right) = 3.71 + 0.133t,$$

where $E_{\text{Matrix, AC}}$ is in Pa, t is animal age in days ($t = 0$ at E15.5, the time when the incipient matrix starts to form [34], and $t = 6$ at P0, which is equivalent to E21.5), $R^2 = 0.966$, $p < 0.0001$ (Fig. 5a). This translated to a general exponential stiffening of the primitive matrix with animal age,

$$E_{\text{Matrix, AC}} = 5.08 \times 1.357^t\left(\text{kPa}\right),$$

with 95% CI of [3.99 6.46] kPa for the initial value at $t = 0$, α_E, and [1.319 1.396] for the base, β_E (Table 2). In other words, the matrix modulus increased by 35.7% [31.9 39.6]% on a daily basis, $(\beta_E - 1)$,

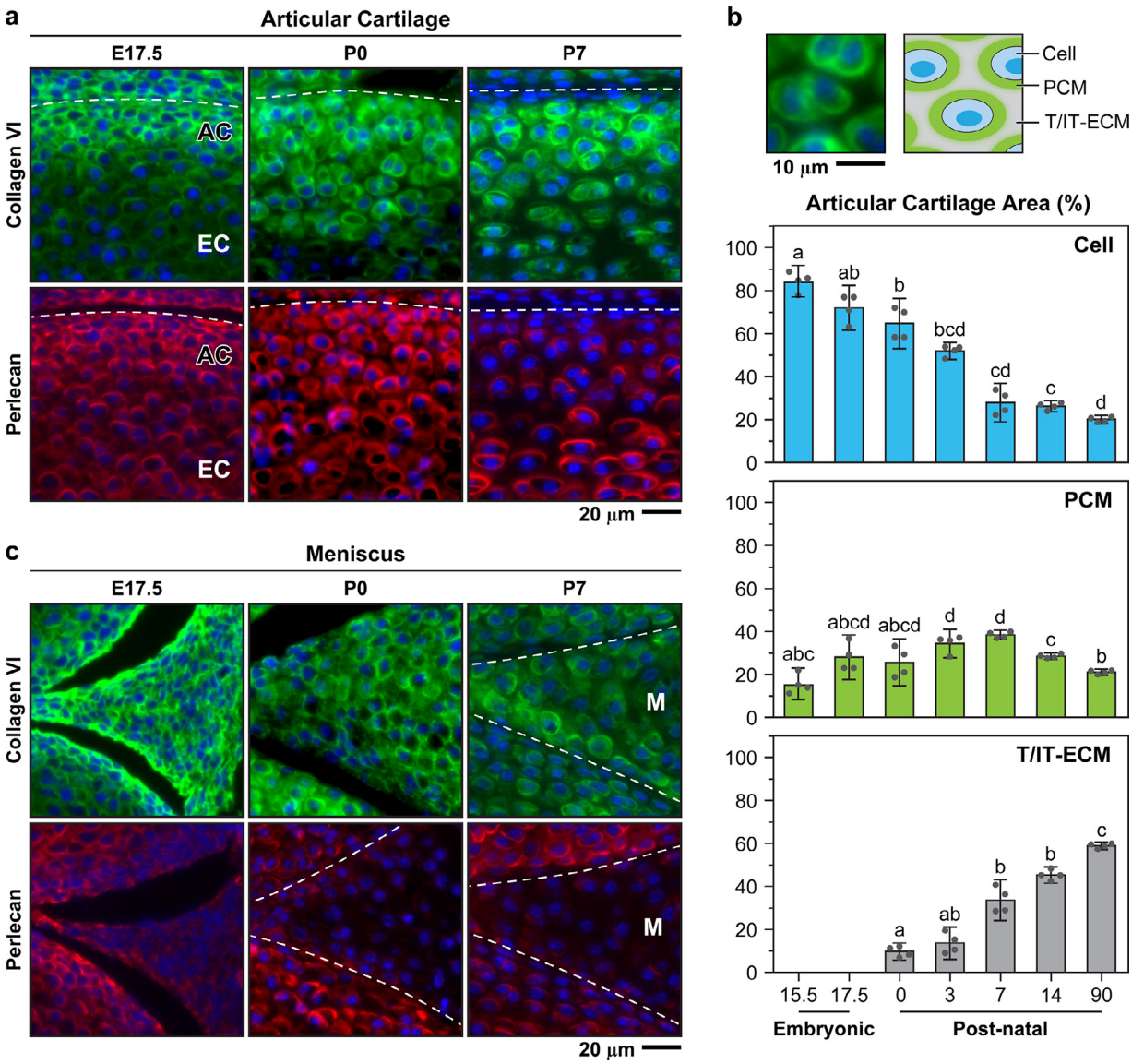

Fig. 2. Separation of PCM and T/IT-ECM domains in the developing primitive matrices of articular cartilage and meniscus. a) High-resolution IF images of PCM biomarkers, collagen VI (green) and perlecan (red; blue: DAPI), at embryonic day 17.5 (E17.5) and post-natal day 0 and 7 (P0 and P7) for articular cartilage (AC: articular cartilage, EC: epiphyseal cartilage, $n = 4$/age). Separation of PCM and T/IT-ECM is visualized from IF images of collagen VI and perlecan at P0 and P7. Dashed lines denote the surface of tibia cartilage. b) Quantification of the area percentage occupied by cell, PCM and T/IT-ECM regions in articular cartilage illustrates gradual changes of the three domains during embryonic and post-natal development (mean ± 95% CI, $n = 4$). Top panel: representative collagen VI IF image at P0 and schematic illustrations that demonstrate the definition of areas corresponding to cell, PCM and T/IT-ECM. Each data point represents the value from one animal, different letters indicate significant age-associated differences ($p < 0.05$). Data from P3, P14 and P90 are adapted from Ref. [50] with permission. c) High-resolution IF images of collagen VI and perlecan at E17.5, P0 and P7 for the meniscus (M, $n = 4$/age). Separation of PCM and T/IT-ECM is visualized from IF images of collagen VI at P7. Dashed lines denote the surface of the meniscus.

from E17.5 to P7. This exponential dependence, however, was not applicable to P14 and P90 (Fig. 5a), suggesting that such rapid stiffening was specific to early stages of cartilage development.

We then confirmed that this exponential stiffening of the primitive matrix started as soon as E15.5, and took place at the length scale representing integrated responses of the matrix and cell remnants as a whole. Applying classical AFM nanoindentation with an indenter tip of $R \approx 12.45$ μm and a contact radius of ≈ 4.9 μm, we also found an exponential dependence of modulus, $E_{\text{Tissue, AC}}$, with age, where $log_{10}(E_{\text{Tissue, AC}}) = 3.60 + 0.113t$, or $E_{\text{Tissue, AC}} = 3.71 \times 1.298^t$ (kPa), representing a daily stiffening rate of 29.8% [27.5 32.1]% (Fig. 6a,b). This stiffening rate was lower than that measured by IF-AFM nanomechanical mapping with the smaller indenter tip ($R \approx 2.25$ μm, Fig. 6c, $p < 0.05$), which may be attributed to the fact that the confounding effects due to the softer regions of cell remnants were not separated by the larger indenter tip [38].

3.5. Distinct stiffening patterns in the primitive matrix of articular cartilage versus meniscus

The stiffening of the meniscus primitive matrix also followed a similar exponential dependence, albeit at a lower rate. From IF-AFM nanomechanical mapping, the modulus of meniscus matrix increased from 12.6 ± 3.9 kPa at E17.5 to 92 ± 50 kPa at P7 (Fig. 4a,b). This 7.4 ± 1.0-fold stiffening was substantially lower than that of cartilage matrix (29.8 ± 2.7-fold). The age-dependence of the matrix micromodulus can be described by the equation,

$$E_{\text{Matrix, M}} = 7.92 \times 1.198^t \left(\text{kPa}\right),$$

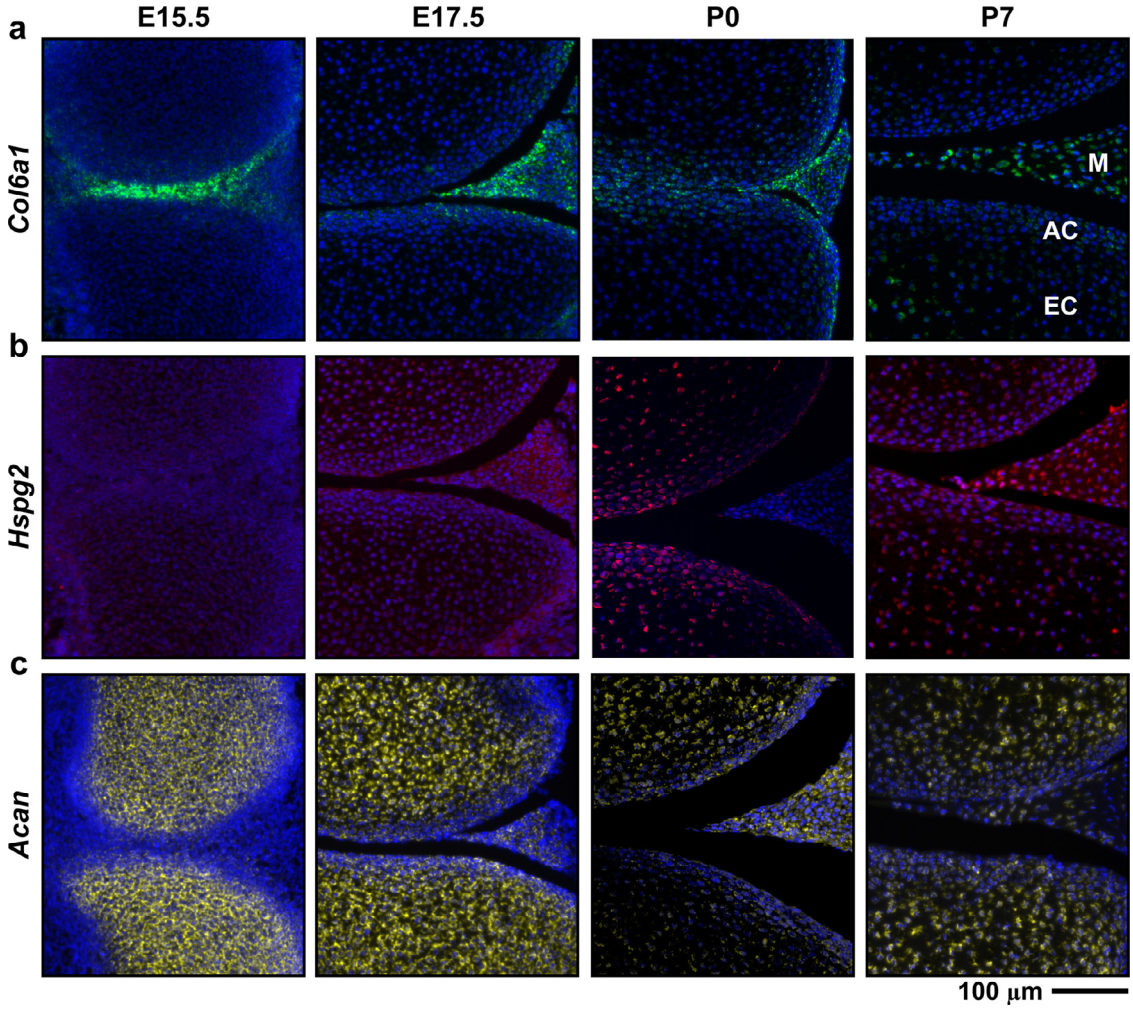

Fig. 3. Spatial distribution of the matrix gene expressions in developing knee joints assessed by RNAscope fluorescent in situ hybridization. a) *Col6a1* (collagen VI, green), b) *Hspg2* (perlecan, red) and c) *Acan* (aggrecan, yellow; blue: Hoechst 33342). Images are taken at embryonic day 15.5 and 17.5 (E15.5 and E17.5) and post-natal day 0 and 7 (P0 and P7) (AC: articular cartilage, EC: epiphyseal cartilage, M: meniscus, $n = 4$/age). *Col6a1* is mainly expressed in articular cartilage and the meniscus while *Hspg2* and *Acan* are expressed throughout all three tissues.

equating to a relative daily stiffening rate of 19.8% [14.9 24.9]% (Fig. 5b). This rate was significantly lower than that of the articular cartilage matrix. Similarly, classical AFM nanoindentation with the larger indenter ($R \approx 12.45$ μm) yielded $E_{\text{Tissue, M}} = 4.54 \times 1.187^t$ (kPa) from E15.5 to P7 with a relative stiffening rate of 18.7% [17.5 20.0]%, which was also lower than that of articular cartilage (29.8% [27.5 32.1]%) measured via the same modality (Fig. 6c).

We also found that epiphyseal cartilage followed a similar stiffening pattern as articular cartilage when tested under the larger indenter tip. From E15.5 to P7, epiphyseal cartilage exhibited a 22.0 ± 0.4-fold increase from 4.67 ± 0.17 kPa at E15.5 to 103.0 ± 4.9 kPa at P7, yielding $E_{\text{Tissue, EC}} = 4.53 \times 1.280^t$ (kPa) (Fig. 6a,b). The relative daily stiffening rate was 28.0% [25.7 30.3]%, similar to that of articular cartilage and higher than that of the meniscus (Fig. 6c). Comparing these three tissues, their moduli all started at a similar range ≈ 5 kPa at E15.5 (Fig. 6a), yielding a similar modulus base, α_E, estimated from the log-linear fit (Fig. 6c). As a result of the differential stiffening rates, however, articular and epiphyseal cartilage became significantly stiffer than the meniscus by P0 and P7 (Figs. 4b, 5a). Thus, the early development of the primitive matrices in all three tissues was characterized by an exponential stiffening trend, but the stiffening rate was much higher in hyaline cartilage (articular and epiphyseal cartilage) than in fibrocartilage (the meniscus).

3.6. Rapid increase in the spatial heterogeneity of developing primitive matrix

Concurrent with the rapid stiffening, we also detected an increase in spatial heterogeneity of the primitive matrix. First, we separated the micromodulus of PCM and T/IT-ECM when these two domains became distinct in articular cartilage at P0 and P7, and in the meniscus at P7. For all three groups, the T/IT-ECM showed significantly higher modulus than the PCM (Fig. 7a). Since the cartilage primitive matrix initiates as a PCM-like template (Fig. 2), we also tested the log-linear dependence of PCM-only micromodulus with age. We confirmed a similar exponential stiffening trend, $E_{\text{PCM, AC}} = 5.05 \times 1.325^t$ (kPa, $R^2 = 0.972$, $p < 0.0001$), or a 32.5% [29.4 35.6]% relative daily stiffening rate. Thus, early development of the primitive matrix is characterized by not only the separation of PCM and T/IT-ECM, but also the rapid stiffening of both the immediate cell niche and the matrix bulk as a whole. In addition to the separation of PCM and T/IT-ECM, we also observed a gradual increase in the heterogeneity of matrix modulus in both articular cartilage and the meniscus, as marked by an exponential increase

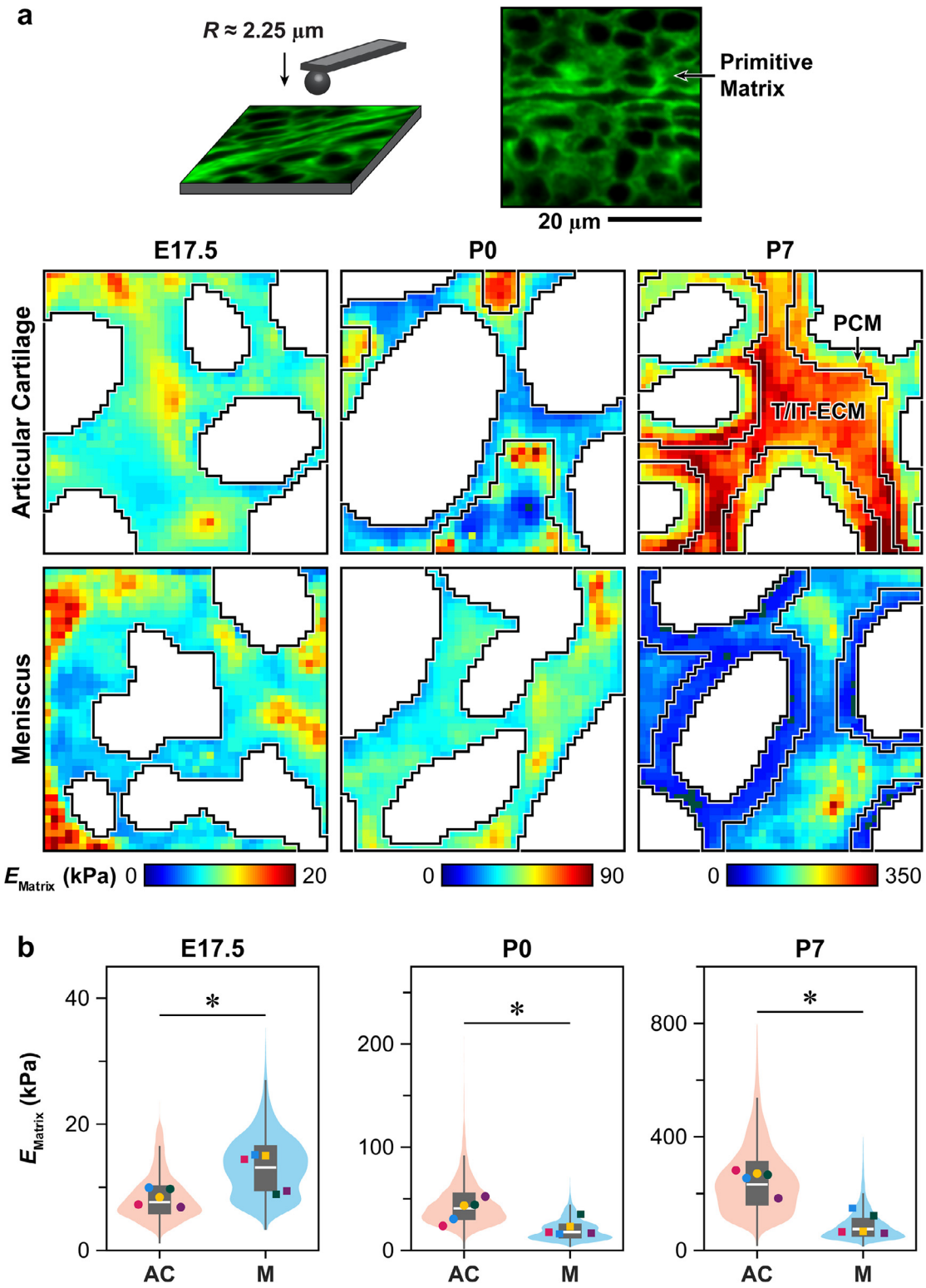

Fig. 4. Rapid stiffening of the primitive matrix in developing articular cartilage and meniscus, as assessed by IF-guided AFM nanomechanical mapping using a microspherical indenter tip ($R \approx 2.25$ µm). a) Top panel: Schematic illustration of IF-guided AFM on the cryo-section of embryonic day 17.5 (E17.5) murine cartilage, with immunolabelling of collagen VI present throughout the intercellular spacing. Bottom panel: Representative 20 × 20 µm^2 maps of indentation modulus, E_{ind}, of the primitive matrix for articular cartilage and the meniscus at E17.5 and post-natal day 0 and 7 (P0 and P7). Domains corresponding to the PCM and T/IT-ECM are separated when applicable, and moduli corresponding to cell remnants are removed (white voids). b) Violin plots of the micromodulus of the primitive matrix, E_{Matrix}, of articular cartilage (AC) and the meniscus (M) at E17.5, P0 and P7 (≥ 1,200 positions tested for each tissue on each animal, from $n = 5$ at each age, *: $p < 0.05$ between articular cartilage and the meniscus). Each data point represents the average micromodulus from one animal. Data points with the same color indicate values measured from the same animal at each age.

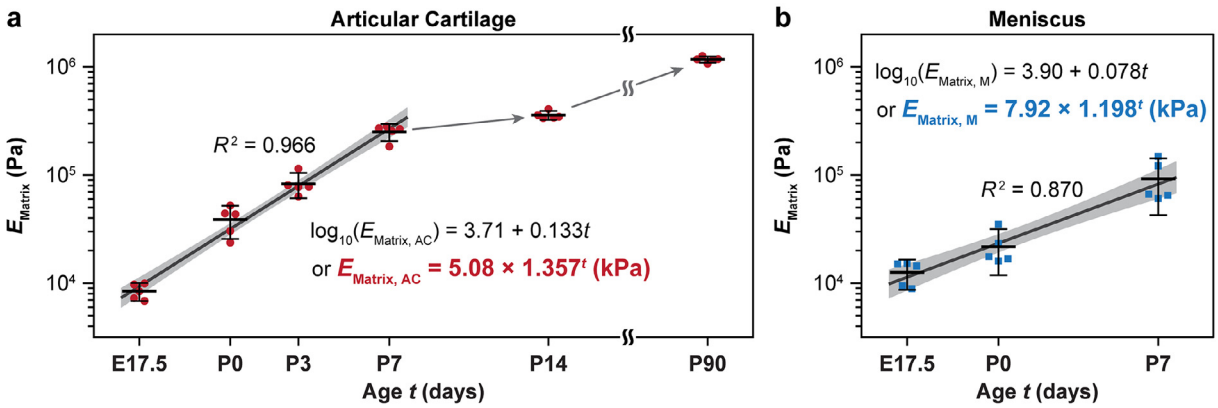

Fig. 5. Exponential increase of the primitive matrix modulus with age, as assessed by immunofluorescence (IF)-guided AFM nanomechanical mapping using a microspherical indenter tip ($R \approx 2.25$ µm). Semi-logarithmic plots of the micromodulus of the primitive matrix, E_{Matrix}, versus animal age t (in days, from embryonic day 17.5, E17.5 to post-natal day 90, P90, $t = 0$ at E15.5) of a) articular cartilage (AC) and b) the meniscus (M). Both tissues exhibit exponential increases of E_{Matrix} with age from E17.5 to P7. The least-squares linear regression fit of $log_{10}(E_{Matrix})$ versus t is shown as mean ± 95% CI. Each data point represents the average value from one animal (mean ± 95% CI). Data from P3, P14 and P90 in panel a) are adapted from Ref. [50] with permission.

in the standard deviation of matrix micromodulus, s_E, measured from each map (Fig. 7b). Similar to the trend observed in E_{Matrix}, the values of s_E followed a log-linear dependence with animal age t ($p < 0.0001$, Table 2),

$$s_{E,\ AC} = 1.45 \times 1.402^t\left(\text{kPa}\right),\ \ R^2 = 0.942,$$

$$s_{E,\ M} = 0.96 \times 1.314^t\left(\text{kPa}\right),\ \ R^2 = 0.766.$$

The standard deviation increased by 40.2% [33.3 47.5]% daily for articular cartilage, and by a similar daily rate of 31.4% [20.1 43.8]% for the meniscus ($p = 0.188$ between the two tissues). Furthermore, we calculated the coefficient of variation, or the relative standard deviation, by normalizing s_E with the respective average modulus of each map, and still observed an increasing trend of s_{ER} with age for both tissues (Fig. 7c). This suggested that matrix development was associated with increased complexity and heterogeneity even after the respective baseline (average modulus) at each age was taken into account.

Following collagen VI IF-guided partitioning, we estimated the Euclidean distance between each matrix location to its closest cell surface, $d_{\text{Matrix-to-Cell}}$, within each ROI (Fig. 8a), and applied simple linear regression to E_{Matrix} versus $d_{\text{Matrix-to-Cell}}$ (Table 2),

$$E_{\text{Matrix}} = a_d + b_d \cdot d_{\text{Matrix-to-Cell}}.$$

This regression yielded significant slopes, b_d ($p < 0.001$), with R^2 between 0.20-0.60 (Fig. 8b). Thus, linear regression was able to explain ≈ 20-60% of the total variation in modulus with p-values < 0.001, suggesting that distance to cell surface alone accounts for a substantial proportion of the micromechanical heterogeneity (Fig. 8b).

The slope b_d also increased rapidly with age from E17.5 to P7 (Fig. 8c). We found that the log-linear relationship also held for b_d versus animal age ($p < 0.0001$), where simple linear regression of $\log_{10}(b_d)$ versus animal age t (Table 2) yielded,

$$b_{d,\ AC} = 0.950 \times 1.372^t\left(\text{kPa}/\mu\text{m}\right),\ \ R^2 = 0.918,$$

$$b_{d,\ M} = 0.910 \times 1.241^t\left(\text{kPa}/\mu\text{m}\right),\ \ R^2 = 0.790.$$

This indicated that the local slope of modulus versus matrix-to-cell distance, b_d, increased by 37.2% [30.0 45.2]% daily for articular cartilage, and 24.1% [16.1 32.7]% daily for the meniscus ($p = 0.020$ between the two tissues). These rates were comparable to the daily stiffening rate, ($\beta_E - 1$), and daily increase rate of standard deviation, ($\beta_s - 1$), for each tissue (Fig. 8d). Thus, during early development, the primitive matrix exhibited exponential increases in not only the modulus, but also the spatial heterogeneity as denoted by s_E and b_d. Similar to the contrasts in the daily stiffening rate, ($\beta_E - 1$), the rate of heterogeneity increase, ($\beta_d - 1$), was faster in articular cartilage than in the meniscus (Fig. 8d).

4. Discussion

4.1. Development of the articular cartilage primitive matrix

This study identifies several distinctive traits of the primitive matrix in developing articular cartilage (Fig. 9). First, articular cartilage initiates with a PCM-like primitive matrix immediately surrounding cells and forming the bulk of intercellular spacing (E15.5 and E17.5). This step is followed by a separation into distinct PCM and T/IT-ECM domains at P0, and then, further expansion of the T/IT-ECM until maturity (P90) (Fig. 9a). Second, immediately following the first appearance of matrix at E15.5, the primitive matrix undergoes exponential stiffening, resulting in a nearly 30-fold increase in modulus over a 14-day period (Fig. 9b). This rapid stiffening is specific to the early matrix development, as the exponential growth model does not predict further increases in modulus at later post-natal ages (Fig. 5a). Third, this stiffening is accompanied by a concurrent increase in local heterogeneity of micromechanics, marked by exponential increases in s_E (Fig. 7b) and b_d (Fig. 8c), as well as an increase in s_{ER} (Fig. 7c), underscoring the rapid growth in structural and mechanical complexity in the developing primitive matrix.

This rapid matrix development can be attributed to several molecular events. In IF-AFM nanomechanical mapping, the tip-sample contact radius, ≈ 0.7 µm, is much greater than the size of an individual collagen fibril (≈ 30-80 nm in diameter [50,60]) or chondroitin sulfate (CS)-GAG chains on aggrecan (≈ 30-40 nm in length [74]), we expect the modulus outcomes to represent the integrated responses of these matrix constituents, instead of the properties of individual collagen fibrils or sGAG chains. During development, the formation of cartilage matrix involves continuous deposition and assembly of collagen II fibrils and aggrecan. Increased collagen fibril assembly and lysyl oxidase (LOX)-mediated cross-linking are known to stiffen the fibrillar matrix, as has been shown in embryonic tendon [75]. Besides collagens, the increased deposition and packing of aggrecan molecules could be another major determinant of these mechanical changes. In mature cartilage, the electrical double layer (EDL) repulsion arising from the fixed negative charges on CS-GAGs contributes to ≈ 50-65% of the compressive modulus [76,77]. Within the matrix, the

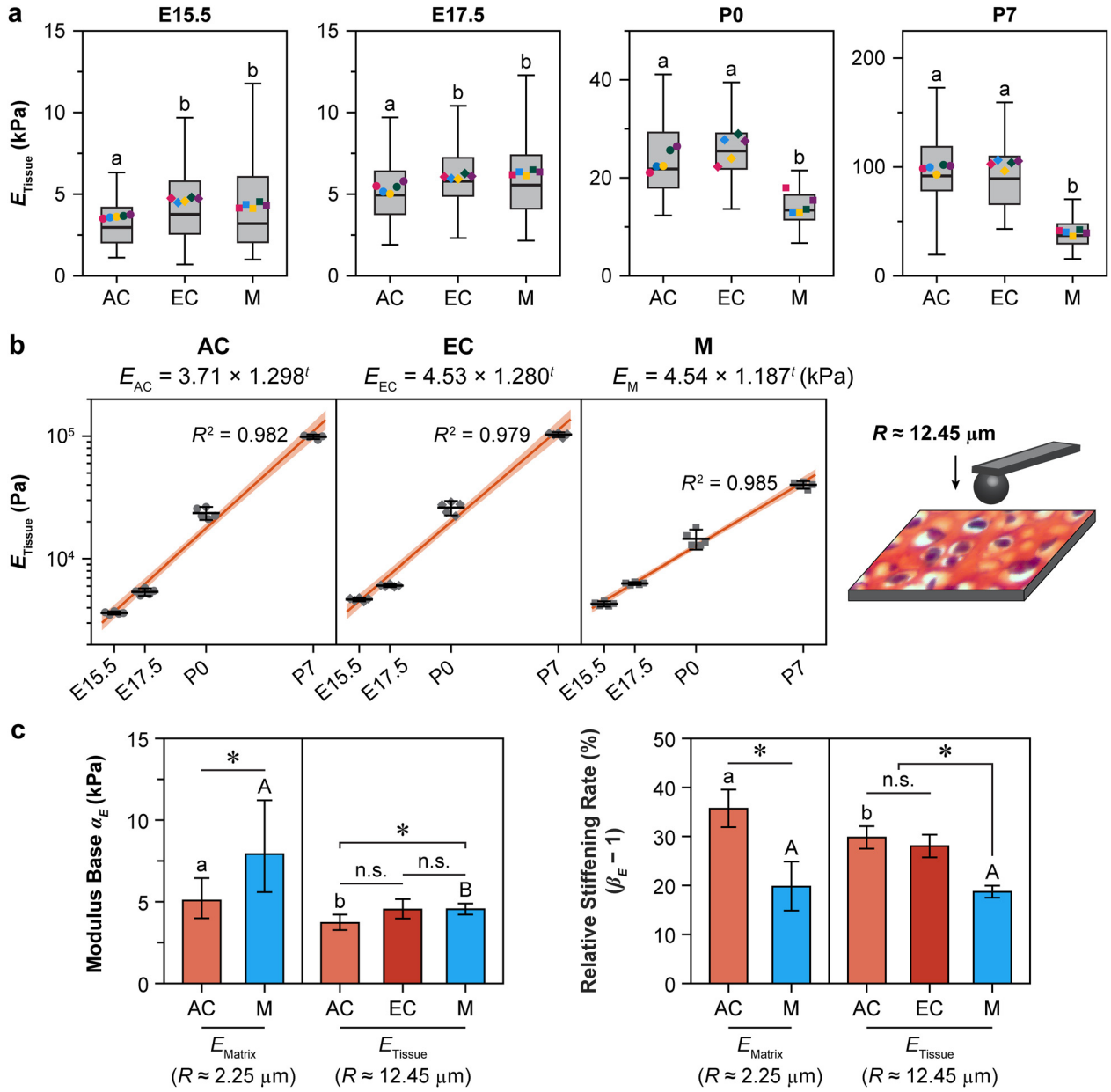

Fig. 6. Rapid stiffening of developing articular cartilage, epiphyseal cartilage and the meniscus, as assessed by classical AFM nanoindentation using a microspherical indenter tip ($R \approx 12.45$ μm). a) Box-and-whisker plot of the micromodulus, E_{Tissue}, of articular cartilage (AC), epiphyseal cartilage (EC) and the meniscus (M) at embryonic day 15.5 and 17.5 (E15.5 and E17.5) and post-natal day 0 and 7 (P0 and P7) ($\geq$ 75 locations from $n = 5$ animals for each age). Each data point represents the average value measured from one animal, different letters indicate significant differences amongst different tissues ($p < 0.05$). Data points with the same color indicate values measured from the same animal at each age. b) Semi-logarithmic plots of the micromodulus, E_{Tissue}, versus animal age t (in days, $t = 0$ at E15.5) show exponential increases of E_{Tissue} with age from E15.5 to P7 for all three tissues. The least-squares linear regression fit of $log_{10}(E_{Tissue})$ versus t is shown as mean ± 95% CI. Each data point represents the average value from one animal (mean ± 95% CI). Right panel inset: Schematic illustration of classical AFM nanoindentation using the microspherical indenter tip. c) Comparisons of the modulus base, α_E (in kPa), and relative daily stiffening rate, ($\beta_E - 1$), derived from the log-linear regression, $E = \alpha_E \cdot \beta_E{}^t$ (in kPa), between the primitive matrices of articular cartilage and meniscus measured by IF-AFM nanomechanical mapping ($R \approx 2.25$ μm), amongst the three tissues measured by classical AFM nanoindentation, as well as between the two different modalities measured on the same tissue. Different letters indicate significant differences between AFM modalities for the same tissue ($p < 0.05$) and *: $p < 0.05$ indicates significant differences amongst different tissues from the same AFM test.

Debye length, κ^{-1}, which characterizes the exponential decay distance of EDL repulsion effect, is $\approx$ 1 nm [78]. This is on the same order of magnitude as the CS-GAG packing distance along aggrecan core protein ($\approx$ 2-3 nm) [74]. As a result, the electrical potential is highly heterogeneous within the tissue. The EDL repulsion thus increases exponentially with CS-GAG packing density, as predicted by the unit cell model [79] or charged rod model [80] that accounts for the nanoscale heterogeneity [78]. Therefore, increased deposition and packing of aggrecan (Fig. 9c, schematics inspired by [40,50,81,82]) can result in exponentially increased EDL repulsion, which may contribute to the observed exponential stiffening. This hypothesis is supported by the similar stiffening trend observed in aggrecan-rich epiphyseal cartilage, and the slower stiffening rate in the meniscus that has less aggrecan content (Fig. 6c).

4.2. Implications for cartilage developmental biology

This study establishes the primitive matrix and its rapid maturation as a key step in cartilage formation (Fig. 9c). In the canonical framework of synovial joint development, the major steps are con-

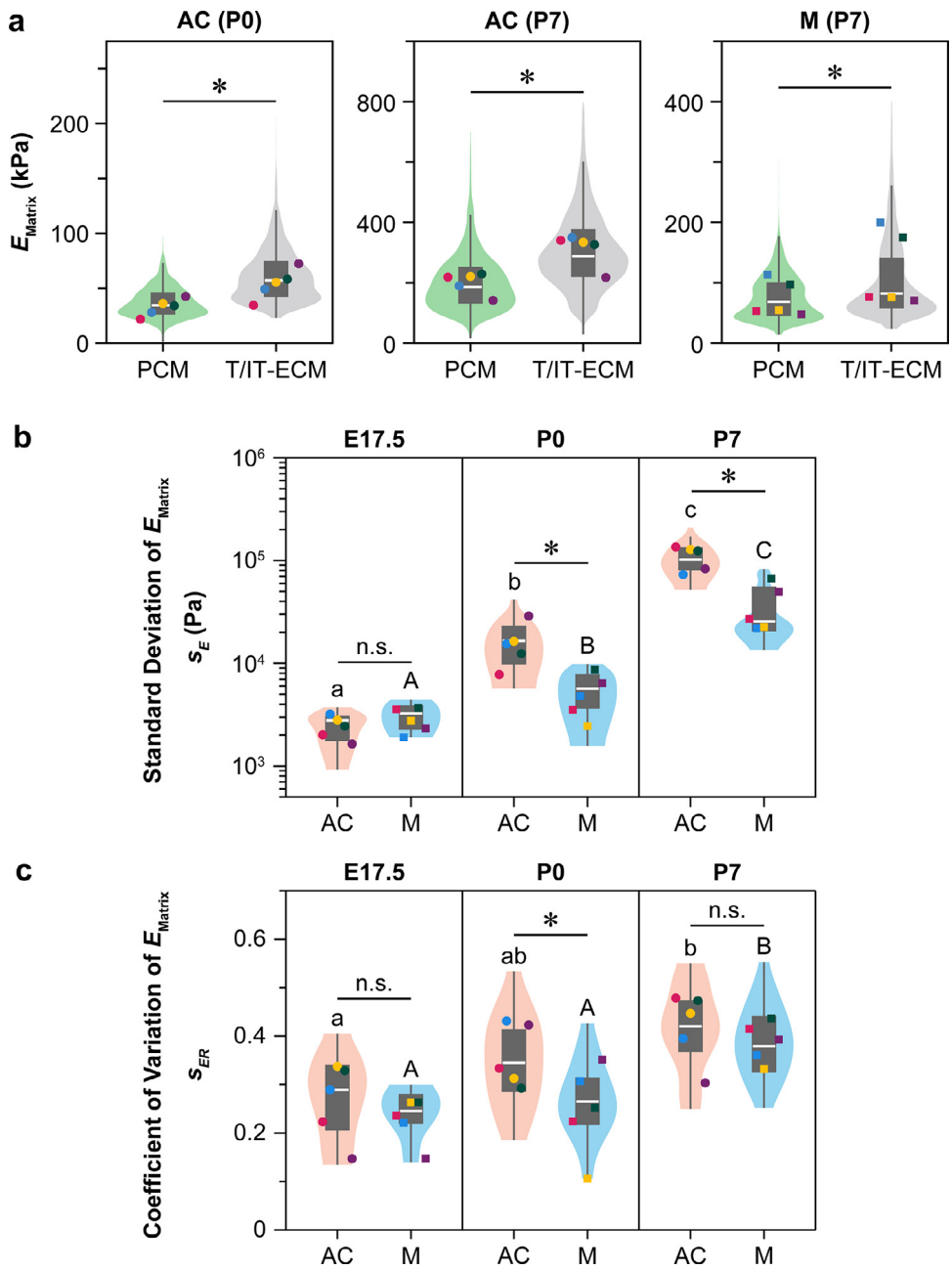

Fig. 7. Increased spatial heterogeneity of the primitive matrix micromechanics in developing articular cartilage and meniscus. a) Violin plots of the micromodulus of PCM and T/IT-ECM measured on articular cartilage (AC), at post-natal days 0 and 7 (P0 and P7) and the meniscus (M) at P7 show higher modulus of the T/IT-ECM domain in all three cases (*: $p < 0.05$ between PCM and T/IT-ECM, ≥ 600 positions tested for each region on each animal, $n = 5$ animals at each age). b) and c) Violin plots of the b) absolute standard deviation, s_E (semi-log plot), and c) coefficient of variation, or relative standard deviation, s_{ER}, measured on articular cartilage and the meniscus from embryonic day 17.5 (E17.5) to P7 (≥ 5 ROIs for each tissue from each animal, $n = 5$ animals at each age). Different letters indicate significant age-associated differences for the same tissue ($p < 0.05$) and *: $p < 0.05$ indicates significant differences between the two tissues at each age. Panels a) – c): Each data point represents the average value measured from one animal. Data points with the same color indicate values measured from the same animal at each age.

sidered to include mesenchymal condensation, interzone specification, cavitation, morphogenesis, and finally, the growth and maturation of joint tissues [4]. Here, we show that the rapid specialization of the primitive matrix starts immediately following the first instance of matrix formation at E15.5, and is hallmarked by a nearly 30-fold stiffening in 14 days, separation of clearly defined PCM and T/IT-ECM domains, and a rapid increase in matrix heterogeneity (Fig. 9b). These activities mark the initial steps that give rise to the hierarchically structured, mechanically functional mature ECM, and take place simultaneously with the well-known processes during morphogenesis, such as cell proliferation, differentiation, swelling, and tissue volume expansion [83]. Clearly, the deposition and assembly of the matrix occurs much faster than the expansion of tissue volume, resulting in an increased packing of matrix molecules, and thus, rapid stiffening of the matrix.

One open question in developmental biology is how articular cartilage retains its permanent status throughout life, rather than being remodeled into bone [84]. Our results show that, in addition to the known differences in their cellular origins and initial gene expression profiles [85], articular cartilage and epiphyseal cartilage

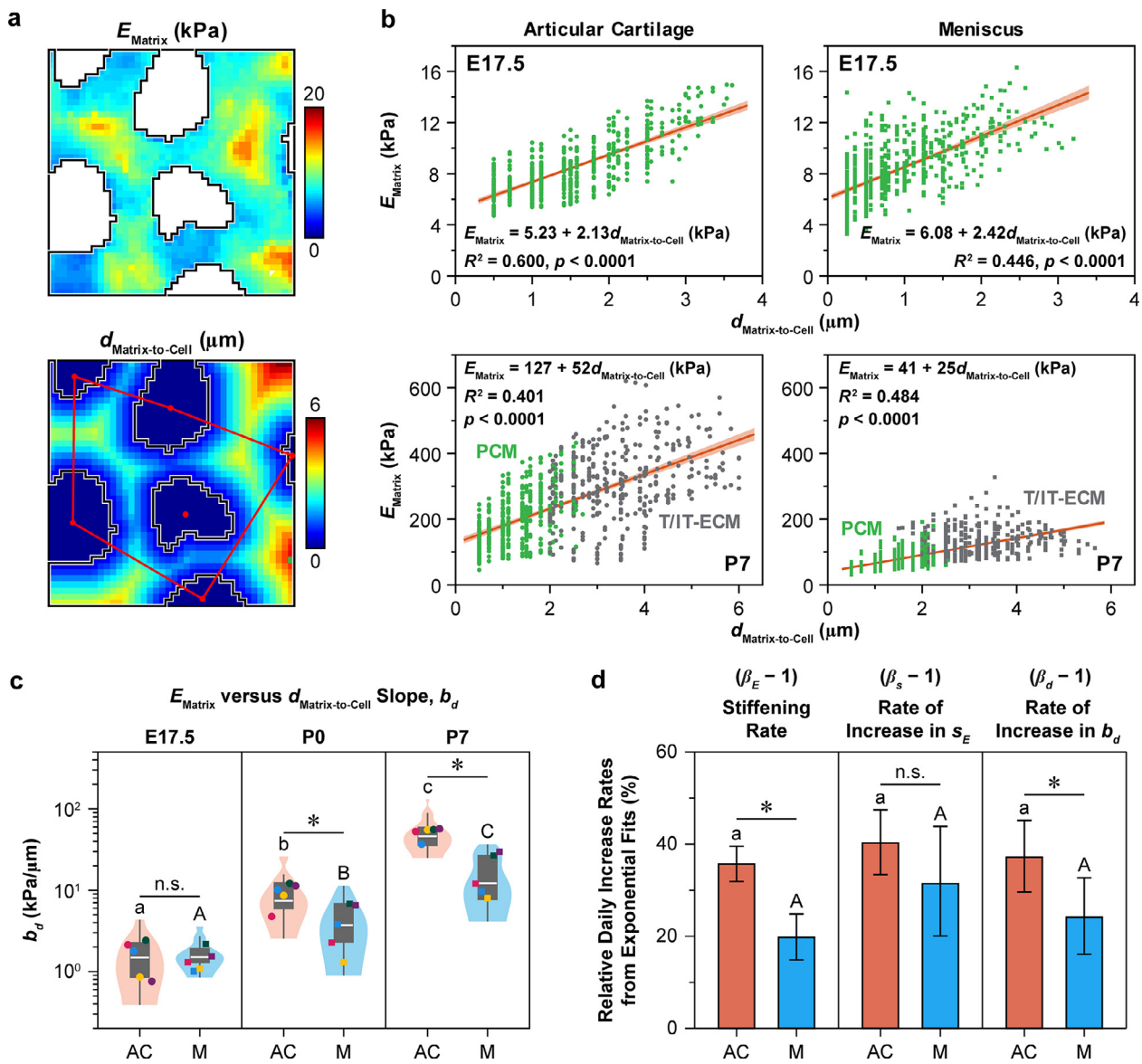

Fig. 8. Increased dependence of the matrix micromodulus with respect to the Euclidean distance to cell surface, $d_{Matrix-to-Cell}$, in the primitive matrices of articular cartilage (AC) and the meniscus (M). a) Representative 20 × 20 μm^2 maps of the cell-to-matrix Euclidean distance estimated based on the IF-labeled collagen VI images and corresponding modulus map of articular cartilage at E17.5. b) Representative least-squares linear regression analysis of E_{Matrix} versus $d_{Matrix-to-Cell}$, $E_{Matrix} = a_d + b_d \cdot d_{Matrix-to-Cell}$, for articular cartilage and the meniscus at embryonic day 17.5 (E17.5) and post-natal day 7 (P7). c) Semi-logarithmic violin plots of the slope of E_{Matrix} versus $d_{Matrix-to-Cell}$, b_d, estimated from all regions of interest (ROIs) measured on the primitive matrix of articular cartilage and the meniscus at E17.5, P0 and P7 (≥ 5 ROIs for each tissue from each animal, $n = 5$ animals at each age). Each data point represents the average b_d measured from one animal (*: $p < 0.05$). Data points with the same color indicate values measured from the same animal at each age. d) Comparison of the three daily increase rates calculated from the exponential fits: the relative daily stiffening rate, denoted as ($\beta_E - 1$), the daily increase rate of s_E, denoted as ($\beta_s - 1$), and the daily increase rate of b_d, denoted as ($\beta_d - 1$), measured on articular cartilage and the meniscus (mean ± 95% CI). The same letter indicates lack of significant differences amongst the three ratios for each tissue ($p > 0.05$) and *: $p < 0.05$ indicates significant differences between articular cartilage and the meniscus for each parameter.

have also developed distinct traits in their initial primitive matrices, as illustrated by their differential expression and deposition of aggrecan and sGAGs (Figs. 1a, 2a and 3c). Despite its lower sGAG content, articular cartilage has a similar modulus as epiphyseal cartilage in all tested ages (Fig. 6a). This is possibly due to differences in their matrix composition and organization, which have compensated for the lower sGAG content in articular cartilage, rather than the residing hypertrophic chondrocytes in epiphyseal cartilage that may have led to a higher cellular volume proportion, *i.e.*, a lower volume proportion of the matrix. Indeed, we did not find significant differences in the areas occupied by the matrices between the two tissues (*e.g.*, 35 ± 12% and 30 ± 9% of matrix area proportions in articular and epiphyseal cartilage at P0, respectively, $n = 4$, $p = 0.322$).

Besides collagen II and aggrecan, cartilage matrix consists of many other collagens, proteoglycans and glycoproteins (Fig. 9c) [81]. In this regard, minor matrix molecules, such as collagen VI (Figs. 1b, 2a) and tenascin [86], are more concentrated in articular cartilage, supporting that the matrix templates of articular versus epiphyseal cartilage are different upon their inception, although both being considered as hyaline cartilage. Our findings thus provide the foundation to further elucidate the mechanisms by which the primitive matrices regulate the permanent versus transient status of hyaline cartilage. To this end, future studies are

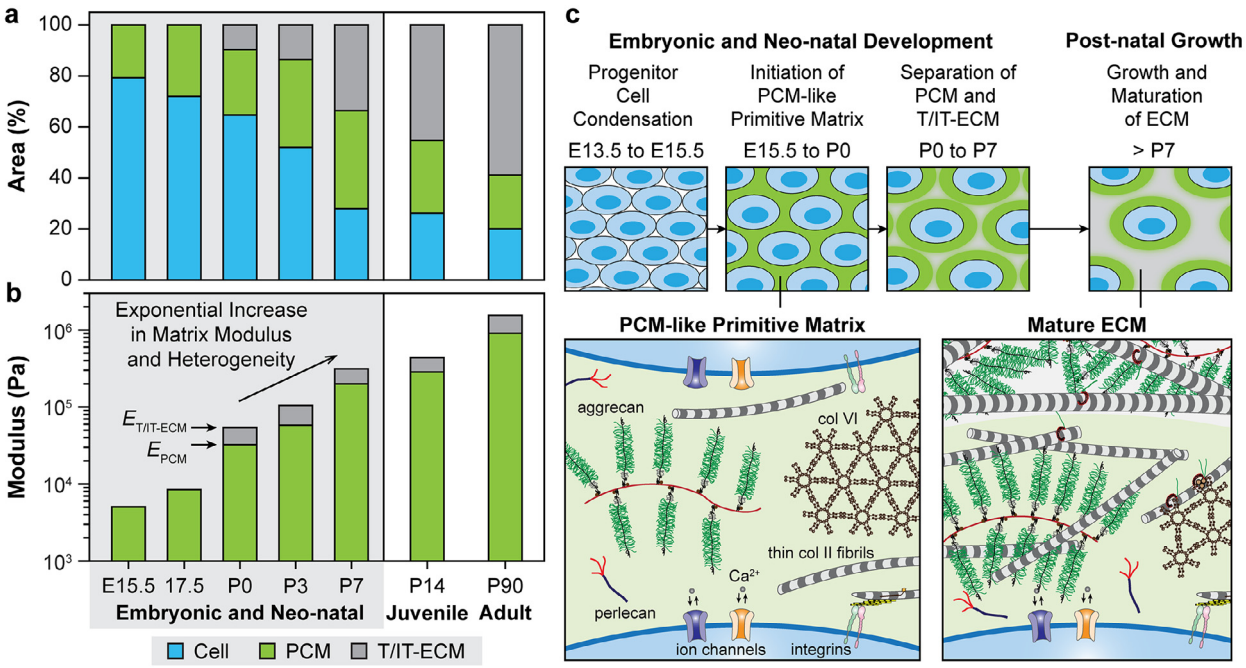

Fig. 9. Schematic illustration of the development of articular cartilage primitive matrix. a) Bar graph of the progressive changes in the area proportions occupied by cells, PCM and T/IT-ECM from embryonic day 15.5 (E15.5) to maturity at post-natal day 90 (P90). b) Semi-logarithmic bar graph of the average modulus of the PCM, and T/IT-ECM when applicable, from E15.5 to P90. The modulus of E15.5 matrix is estimated as the base value, α_E, for articular cartilage calculated from the log-linear regression of E_{Matrix} versus t (Fig. 5a). c) Schematic illustration of the working hypothesis on the key steps and molecular events contributing to the development of articular cartilage primitive matrix. Immediately following progenitor cell condensation, articular cartilage initiates with a PCM-like primitive matrix during embryonic development. This is followed by the separation of PCM and T/IT-ECM, and further expansion of the T/IT-ECM domain up to maturity. In this process, the increased deposition, assembly and packing of ECM molecules, including collagen II fibrils and aggrecan, contribute to the rapid, exponential stiffening of the developing primitive matrix from E15.5 to P7. The schematics are inspired by Ref. [40,50,81,82].

required to discern the composition and distributions of other matrix molecules between these two units in a more systematic fashion, as well as to uncover the individual and coordinated roles of regulatory matrix molecules.

4.3. Implications for cartilage tissue engineering

In tissue engineering, one guiding principle is to recapitulate the key steps of native tissue development to form functional tissue replacements [10]. To this end, scaffold-less condensed mesenchymal cell bodies (CMBs) have been used to mimic the mesenchymal condensation step in vivo. This approach successfully generated engineered cartilage products with an elastic modulus ≈ 850 kPa over 5 weeks of culture in vitro [87], which indicates an average ≈ 16% daily stiffening assuming an initial modulus of ≈ 5 kPa. Here, we show that the stiffening of native matrix in vivo can be even faster, with a daily modulus increase of ≈ 36%. This suggests that a better understanding and recapitulation of this native in vivo process could be further leveraged to accelerate the building of native tissue-like products. In addition, decellularized ECM (dECM) is a popular class of biomaterials for cartilage repair, thanks to its capability of providing a physiological-like microenvironment [88]. The dECMs derived from younger tissues or cells often show advantageous regenerative outcomes. However, aberrant ectopic calcification has been reported for dECMs derived from fetal cartilage [89]. Our results suggest that separating the dECM of articular and epiphyseal cartilage could potentially better retain the permanent status of cartilage and reduce unintended calcification. In this regard, one limitation of the murine model is that murine cartilage lacks the depth-dependent structural heterogeneity observed in human cartilage due to its small thickness (≈ 50 μm-thick in adult mice [90]). Building on findings from this study, our ongoing work investigating the embryonic development of larger animals will provide direct insights for the regenerative products to recapitulate the structural complexity of human articular cartilage. Lastly, chondrocytes and chondroprogenitors are highly mechanosensitive, and often require a soft microenvironment to maintain their chondrogenic phenotype in vitro [91]. In vivo, however, chondrocytes retain their normal homeostasis within this rapidly stiffening microenvironment (Figs. 4, 5). Future work will thus seek to uncover the cell-matrix interactions in this critical development phase, which could guide the design of engineering strategies to better maintain the chondrogenic phenotype while improving the biomechanical functions of regenerative products.

4.4. Development of the meniscus primitive matrix

This study also identifies several distinct features of the primitive matrices in the meniscus versus articular cartilage. First, the slower stiffening of the meniscus matrix could be attributed to differences in their matrix composition and structure, including higher collagen I, lower collagen II and proteoglycan content, as well as different collagen fiber organizations in the meniscus [8]. Such contrast supports our hypothesis that sGAGs and their EDL repulsion are a major factor in the rapid stiffening observed in articular cartilage. It is worth noting that embryonic meniscus expresses higher levels of LOX than articular cartilage [92]. It thus appears that the assembly and pressurization of sGAGs outweigh the effect of LOX-mediated collagen cross-linking in developing primitive matrices. Second, the separation of meniscus PCM and T/IT-ECM takes place at a later time point, *e.g.*, P7 (Fig. 2c), suggesting delayed matrix specialization relative to articular cartilage. Despite sharing similar origins of interzone progenitors as articular

cartilage, meniscus cells show distinct gene expression signatures compared to articular chondrocytes as early as the embryonic stage [93]. Such differences in cell fate and gene expressions corroborate the observed distinctions in the biosynthesis and assembly of their primitive matrices. Third, although perlecan is present in the PCM of mature meniscus [94], the primitive matrix of meniscus shows low concentration of perlecan in comparison to that of both articular and epiphyseal cartilage. In cartilage, perlecan is required for *Sox9*-mediated chondrogenic differentiation during embryonic development [95], and also serves as a chondrocyte mechanotransducer to regulate fibroblast growth factor-2 (FGF-2)-dependent activation of extracellular regulated kinase (ERK) signaling in chondrocytes [96]. The absence of perlecan in developing meniscus thus further supports distinct signaling pathways and cell-matrix interactions in hyaline cartilage versus fibrocartilage. Thus, at its inception, the initial matrix of the meniscus is already different from that of articular cartilage, even before the onset of extensive post-natal physiological joint loading. Given the paucity of knowledge on the molecular activities that regulate the meniscus matrix development, future work is needed to uncover the molecular roles of each matrix constituent, such as collagen VI, perlecan and others, in the formation and maturation of the meniscus matrix.

There are several limitations with regard to the development of the meniscus matrix. First, although separation of the PCM and T/IT-ECM does eventually take place in the meniscus (Fig. 2), we are not able to establish the roadmap of meniscus matrix development similar to that of articular cartilage (Fig. 9). This is due to the scarcity of literature on meniscus matrix development. Even though the appearance of PCM in the meniscus is well known [36], the structure-mechanics principles and mechanobiological functions of the meniscus PCM have not been studied even in mature tissue. Also, given that the separation of PCM and T/IT-ECM takes place during post-natal growth, it is unclear whether the PCM is an anabolic manifestation of cellular responses to physiological compressive loading, or, similar to the case of cartilage, is the initial matrix template pre-specified before the onset of joint loading. Second, we have not delineated the regional heterogeneity of the meniscus primitive matrix. Meniscus cells establish distinct zonal-dependent gene signatures even at the embryonic stage [93]. Mature meniscus matrix is characterized by a highly anisotropic collagen I-dominated fibrous outer zone and a more hyaline-like inner zone with higher collagen II and proteoglycan content [8], as well as the presence of proteoglycan-rich microdomains throughout the tissue [97]. In this study, we focus on the outer zone in order to highlight the differences between the primitive matrices of hyaline cartilage versus fibrocartilage, but have not elucidated the zonal variations or structural anisotropy within the meniscus. Also, similar to the case of articular cartilage, murine meniscus lacks the structural heterogeneity and zonal variations observed in human and larger animals [98]. To address these limitations, building on this work, our ongoing studies aim to query the longitudinal changes in the meniscus PCM and T/IT-ECM biomechanics, mechanosensitive signaling of residing cells, as well as the zonal heterogeneity and anisotropy from embryonic to mature ages in both murine and larger animal models. This will help establish the basis for guiding the regeneration of the meniscus and possibly other fibrocartilage tissues with similar structural complexity.

5. Conclusions

This study highlights the rapid development of the primitive matrix as a crucial step in the establishment of native articular cartilage and meniscus. Immediately after joint cavitation, articular cartilage initiates with a PCM-like primitive matrix occupying the intercellular space. During embryonic and neo-natal development, the primitive matrix undergoes exponential stiffening, with a $\approx$ 36% daily increase in modulus and a concurrent exponential increase in local heterogeneity, as well as a rapid specialization into distinct PCM and T/IT-ECM domains. Also, at this early stage, articular cartilage develops molecular traits that are distinct from the epiphyseal cartilage, indicating that its status as permanent cartilage is already pre-determined at the inception of the primitive matrix. We also observe the exponential matrix stiffening and rapid specialization in the meniscus, albeit at a lower rate of $\approx$ 20%, underscoring distinct matrix development routes for hyaline cartilage versus fibrocartilage. Collectively, these results establish a foundation for understanding the development of native articular cartilage and meniscus ECMs. This enables further studies to investigate how the residing cells maintain their phenotype and metabolic activities within this rapidly stiffening matrix during embryonic and neo-natal growth, and to query the roles of individual matrix and cellular constituents in mediating the dynamic cell-matrix cross-talk. Such knowledge will guide the design of regenerative strategies to recapitulate the key developmental steps in vivo, thus effectively restoring the function of these native tissues.

Declaration of Competing Interests

The authors declare that they have no known competing financial interests or personal relationships that could have appeared to influence the work reported in this paper.

Acknowledgements

This work was financially supported by the National Science Foundation (NSF) Grant CMMI-2047073 (to LH), National Institutes of Health (NIH) Grant R01AR075418 (to RLM and EK), as well as NIH Grant P30AR069619 to the Penn Center for Musculoskeletal Disorders. We thank the Singh Center for Nanotechnology at the University of Pennsylvania for the use of TIRF MFP-3D, which is part of the National Nanotechnology Coordinated Infrastructure Program supported by the NSF Grant NNCI-1542153. All imaging was performed at Drexel University's Cell Imaging Center.

References

[1] A. Cui, H. Li, D. Wang, J. Zhong, Y. Chen, H. Lu, Global, regional prevalence, incidence and risk factors of knee osteoarthritis in population-based studies, EClinicalMedicine 29-30 (2020) 100587.
[2] H. Kwon, W.E. Brown, C.A. Lee, D. Wang, N. Paschos, J.C. Hu, K.A. Athanasiou, Surgical and tissue engineering strategies for articular cartilage and meniscus repair, Nat. Rev. Rheumatol. 15 (2019) 550–570.
[3] E. Koyama, Y. Shibukawa, M. Nagayama, H. Sugito, B. Young, T. Yuasa, T. Okabe, T. Ochiai, N. Kamiya, R.B. Rountree, D.M. Kingsley, M. Iwamoto, M. Enomoto-Iwamoto, M. Pacifici, A distinct cohort of progenitor cells participates in synovial joint and articular cartilage formation during mouse limb skeletogenesis, Dev. Biol. 316 (2008) 62–73.
[4] M. Pacifici, E. Koyama, M. Iwamoto, Mechanisms of synovial joint and articular cartilage formation: recent advances, but many lingering mysteries, Birth Defects Res. C Embryo Today 75 (2005) 237–248.
[5] G. Hyde, R.P. Boot-Handford, G.A. Wallis, *Col2a1* lineage tracing reveals that the meniscus of the knee joint has a complex cellular origin, J. Anat. 213 (2008) 531–538.
[6] Y. Shwartz, S. Viukov, S. Krief, E. Zelzer, Joint development involves a continuous influx of Gdf5-positive cells, Cell Rep. 15 (2016) 2577–2587.
[7] L. Han, A.J. Grodzinsky, C. Ortiz, Nanomechanics of the cartilage extracellular matrix, Annu. Rev. Mater. Res. 41 (2011) 133–168.
[8] E.A. Makris, P. Hadidi, K.A. Athanasiou, The knee meniscus: structure-function, pathophysiology, current repair techniques, and prospects for regeneration, Biomaterials 32 (2011) 7411–7431.
[9] E.A. Kiyotake, E.C. Beck, M.S. Detamore, Cartilage extracellular matrix as a biomaterial for cartilage regeneration, Ann. N. Y. Acad. Sci. 1383 (2016) 139–159.
[10] J.C. Bernhard, G. Vunjak-Novakovic, Should we use cells, biomaterials, or tissue engineering for cartilage regeneration? Stem Cell Res. Ther. 7 (2016) 56.
[11] W. Wang, D. Rigueur, K.M. Lyons, TGFβ signaling in cartilage development and maintenance, Birth Defects Res. C Embryo Today 102 (2014) 37–51.
[12] C. Mundy, T. Yasuda, T. Kinumatsu, Y. Yamaguchi, M. Iwamoto, M. Enomoto-Iwamoto, E. Koyama, M. Pacifici, Synovial joint formation requires local Ext1 expression and heparan sulfate production in developing mouse embryo limbs and spine, Dev. Biol. 351 (2011) 70–81.

[13] Y. Deng, A. Wu, P. Li, G. Li, L. Qin, H. Song, K.K. Mak, Yap1 regulates multiple steps of chondrocyte differentiation during skeletal development and bone repair, Cell Rep 14 (2016) 2224–2237.
[14] R.F. Loeser, Integrins and chondrocyte-matrix interactions in articular cartilage, Matrix Biol. 39 (2014) 11–16.
[15] C. Parisi, V.V. Chandaria, N.C. Nowlan, Blocking mechanosensitive ion channels eliminates the effects of applied mechanical loading on chick joint morphogenesis, Philos. Trans. R. Soc. Lond. B Biol. Sci. 373 (2018).
[16] D.E. Pazin, L.W. Gamer, K.A. Cox, V. Rosen, Molecular profiling of synovial joints: use of microarray analysis to identify factors that direct the development of the knee and elbow, Dev. Dyn. 241 (2012) 1816–1826.
[17] L.W. Gamer, S. Pregizer, J. Gamer, M. Feigenson, A. Ionescu, Q. Li, L. Han, V. Rosen, The Role of Bmp2 in the maturation and maintenance of the murine knee joint, J. Bone Miner. Res. 33 (2018) 1708–1717.
[18] Y. Wei, H. Sun, T. Gui, L. Yao, L. Zhong, W. Yu, S.J. Heo, L. Han, N.A. Dyment, X.S. Liu, Y. Zhang, E. Koyama, F. Long, M.H. Zgonis, R.L. Mauck, J. Ahn, L. Qin, The critical role of Hedgehog-responsive mesenchymal progenitors in meniscus development and injury repair, eLife 10 (2021) e62917.
[19] B. Mikic, A.L. Isenstein, A. Chhabra, Mechanical modulation of cartilage structure and function during embryogenesis in the chick, Ann. Biomed. Eng. 32 (2004) 18–25.
[20] R.C. Solem, B.F. Eames, M. Tokita, R.A. Schneider, Mesenchymal and mechanical mechanisms of secondary cartilage induction, Dev. Biol. 356 (2011) 28–39.
[21] K.A. Roddy, P.J. Prendergast, P. Murphy, Mechanical influences on morphogenesis of the knee joint revealed through morphological, molecular and computational analysis of immobilised embryos, PLoS One 6 (2011) e17526.
[22] V.V. Chandaria, J. McGinty, N.C. Nowlan, Characterising the effects of in vitro mechanical stimulation on morphogenesis of developing limb explants, J. Biomech. 49 (2016) 3635–3642.
[23] T.K. Tsinman, Y. Huang, S. Ahmed, A.L. Levillain, M.K. Evans, X. Jiang, N.C. Nowlan, N.A. Dyment, R.L. Mauck, Lack of skeletal muscle contraction disrupts fibrous tissue morphogenesis in the developing murine knee, J. Orthop. Res. (2023) Under review.
[24] T.D. Brown, R.J. Singerman, Experimental determination of the linear biphasic constitutive coefficients of human fetal proximal femoral chondroepiphysis, J. Biomech. 19 (1986) 597–605.
[25] T.J. Klein, M. Chaudhry, W.C. Bae, R.L. Sah, Depth-dependent biomechanical and biochemical properties of fetal, newborn, and tissue-engineered articular cartilage, J. Biomech. 40 (2007) 182–190.
[26] A.K. Williamson, A.C. Chen, K. Masuda, E.J. Thonar, R.L. Sah, Tensile mechanical properties of bovine articular cartilage: variations with growth and relationships to collagen network components, J. Orthop. Res. 21 (2003) 872–880.
[27] W.E. Brown, G.D. DuRaine, J.C. Hu, K.A. Athanasiou, Structure-function relationships of fetal ovine articular cartilage, Acta Biomater 87 (2019) 235–244.
[28] M. Wong, M. Ponticiello, V. Kovanen, J.S. Jurvelin, Volumetric changes of articular cartilage during stress relaxation in unconfined compression, J. Biomech. 33 (2000) 1049–1054.
[29] R. Mahmoodian, J. Leasure, P. Philip, N. Pleshko, F. Capaldi, S. Siegler, Changes in mechanics and composition of human talar cartilage anlagen during fetal development, Osteoarthritis Cartilage 19 (2011) 1199–1209.
[30] S. Bansal, J.M. Peloquin, N.M. Keah, O.C. O'Reilly, D.M. Elliott, R.L. Mauck, M.H. Zgonis, Structure, function, and defect tolerance with maturation of the radial tie fiber network in the knee meniscus, J. Orthop. Res. 38 (2020) 2709–2720.
[31] X. Xu, Z. Li, L. Cai, S. Calve, C.P. Neu, Mapping the nonreciprocal micromechanics of individual cells and the surrounding matrix within living tissues, Sci. Rep. 6 (2016) 24272.
[32] X. Xu, Z. Li, Y. Leng, C.P. Neu, S. Calve, Knockdown of the pericellular matrix molecule perlecan lowers *in situ* cell and matrix stiffness in developing cartilage, Dev. Biol. 418 (2016) 242–247.
[33] Q. Li, C. Wang, B. Han, F. Qu, H. Qi, C.Y. Li, R.L. Mauck, L. Han, Impacts of maturation on the micromechanics of the meniscus extracellular matrix, J. Biomech. 72 (2018) 252–257.
[34] M. Kim, E. Koyama, C.M. Saunders, W. Querido, N. Pleshko, M. Pacifici, Synovial joint cavitation initiates with microcavities in interzone and is coupled to skeletal flexion and elongation in developing mouse embryo limbs, Biol. Open 11 (2022) bio059381.
[35] R.E. Wilusz, J. Sanchez-Adams, F. Guilak, The structure and function of the pericellular matrix of articular cartilage, Matrix Biol 39 (2014) 25–32.
[36] J. Sanchez-Adams, R.E. Wilusz, F. Guilak, Atomic force microscopy reveals regional variations in the micromechanical properties of the pericellular and extracellular matrices of the meniscus, J. Orthop. Res. 31 (2013) 1218–1225.
[37] F. Guilak, R.J. Nims, A. Dicks, C.L. Wu, I. Meulenbelt, Osteoarthritis as a disease of the cartilage pericellular matrix, Matrix Biol 71-72 (2018) 40–50.
[38] D.R. Chery, B. Han, Q. Li, Y. Zhou, S.J. Heo, B. Kwok, P. Chandrasekaran, C. Wang, L. Qin, X.L. Lu, D. Kong, M. Enomoto-Iwamoto, R.L. Mauck, L. Han, Early changes in cartilage pericellular matrix micromechanobiology portend the onset of post-traumatic osteoarthritis, Acta Biomater 111 (2020) 267–278.
[39] T.L. Vincent, O. McClurg, L. Troeberg, The extracellular matrix of articular cartilage controls the bioavailability of pericellular matrix-bound growth factors to drive tissue homeostasis and repair, Int. J. Mol. Sci. 23 (2022) 6003.
[40] D.E. Birk, P. Brückner, Collagens, suprastructures, and collagen fibril assembly, in: R.P. Mecham (Ed.), The Extracellular Matrix: an Overview, Springer-Verlag, Berlin, 2011, pp. 77–115.
[41] W. Knudson, S. Ishizuka, K. Terabe, E.B. Askew, C.B. Knudson, The pericellular hyaluronan of articular chondrocytes, Matrix Biol 78-79 (2019) 32–46.
[42] M.T. Bayliss, S. Howat, C. Davidson, J. Dudhia, The organization of aggrecan in human articular cartilage. Evidence for age-related changes in the rate of aggregation of newly synthesized molecules, J. Biol. Chem. 275 (2000) 6321–6327.
[43] A. Porter, L. Wang, L. Han, X.L. Lu, Bio-orthogonal click chemistry methods to evaluate the metabolism of inflammatory challenged cartilage after traumatic overloading, ACS Biomater. Sci. Eng. 8 (2022) 2564–2573.
[44] C.A. Poole, S. Ayad, J.R. Schofield, Chondrons from articular cartilage: I. Immunolocalization of type VI collagen in the pericellular capsule of isolated canine tibial chondrons, J. Cell Sci. 90 (1988) 635–643.
[45] N. SundarRaj, D. Fite, S. Ledbetter, S. Chakravarti, J.R. Hassell, Perlecan is a component of cartilage matrix and promotes chondrocyte attachment, J. Cell Sci. 108 (1995) 2663–2672.
[46] L. Han, E.H. Frank, J.J. Greene, H.-Y. Lee, H.-H.K. Hung, A.J. Grodzinsky, C. Ortiz, Time-dependent nanomechanics of cartilage, Biophys. J. 100 (2011) 1846–1854.
[47] N. Ortega, D.J. Behonick, Z. Werb, Matrix remodeling during endochondral ossification, Trends Cell Biol 14 (2004) 86–93.
[48] J. Endicott, P. Holden, J. Fitzgerald, Authentication of collagen VI antibodies, BMC Res. Notes 10 (2017) 358.
[49] I. Arganda-Carreras, V. Kaynig, C. Rueden, K.W. Eliceiri, J. Schindelin, A. Cardona, H.Sebastian Seung, Trainable Weka Segmentation: a machine learning tool for microscopy pixel classification, Bioinformatics 33 (2017) 2424–2426.
[50] D.R. Chery, B. Han, Y. Zhou, C. Wang, S.M. Adams, P. Chandrasekaran, B. Kwok, S.-J. Heo, M. Enomoto-Iwamoto, X.L. Lu, D. Kong, R.V. Iozzo, D.E. Birk, R.L. Mauck, L. Han, Decorin regulates cartilage pericellular matrix micromechanobiology, Matrix Biol 96 (2021) 1–17.
[51] E. Koyama, C. Mundy, C. Saunders, J. Chung, S.E. Catheline, D. Rux, M. Iwamoto, M. Pacifici, Premature growth plate closure caused by a Hedgehog cancer drug is preventable by co-administration of a retinoid antagonist in mice, J. Bone Miner. Res. 36 (2021) 1387–1402.
[52] T. Kawamoto, K. Kawamoto, Preparation of thin frozen sections from nonfixed and undecalcified hard tissues using Kawamot's film method, Methods Mol. Biol. 1130 (2014) (2012) 149–164.
[53] R.E. Wilusz, L.E. DeFrate, F. Guilak, Immunofluorescence-guided atomic force microscopy to measure the micromechanical properties of the pericellular matrix of porcine articular cartilage, J. R. Soc. Interface 9 (2012) 2997–3007.
[54] R.S. Chadwick, Axisymmetric indentation of a thin incompressible elastic layer, SIAM J. Appl. Math. 62 (2002) 1520–1530.
[55] D.C. Lin, D.I. Shreiber, E.K. Dimitriadis, F. Horkay, Spherical indentation of soft matter beyond the Hertzian regime: numerical and experimental validation of hyperelastic models, Biomech. Model. Mechanobiol. 8 (2009) 345–358.
[56] E.K. Dimitriadis, F. Horkay, J. Maresca, B. Kachar, R.S. Chadwick, Determination of elastic moduli of thin layers of soft material using the atomic force microscope, Biophys. J. 82 (2002) 2798–2810.
[57] M.D. Buschmann, Y.-J. Kim, M. Wong, E. Frank, E.B. Hunziker, A.J. Grodzinsky, Stimulation of aggrecan synthesis in cartilage explants by cyclic loading is localized to regions of high interstitial fluid flow, Arch. Biochem. Biophys. 366 (1999) 1–7.
[58] M.A. Sweigart, C.F. Zhu, D.M. Burt, P.D. deHoll, C.M. Agrawal, T.O. Clanton, K.A. Athanasiou, Intraspecies and interspecies comparison of the compressive properties of the medial meniscus, Ann. Biomed. Eng. 32 (2004) 1569–1579.
[59] Q. Li, F. Qu, B. Han, C. Wang, H. Li, R.L. Mauck, L. Han, Micromechanical anisotropy and heterogeneity of the meniscus extracellular matrix, Acta Biomater 54 (2017) 356–366.
[60] B. Han, Q. Li, C. Wang, P. Patel, S.M. Adams, B. Doyran, H.T. Nia, R. Oftadeh, S. Zhou, C.Y. Li, X.S. Liu, X.L. Lu, M. Enomoto-Iwamoto, L. Qin, R.L. Mauck, R.V. Iozzo, D.E. Birk, L. Han, Decorin regulates the aggrecan network integrity and biomechanical functions of cartilage extracellular matrix, ACS Nano 13 (2019) 11320–11333.
[61] K.L. Johnson, Contact Mechanics, Cambridge University Press, Cambridge, 1985.
[62] T.D.B. Jacobs, B. Gotsmann, M.A. Lantz, R.W. Carpick, On the application of transition state theory to atomic-scale wear, Tribol. Lett. 39 (2010) 257–271.
[63] K.L. Cooper, S. Oh, Y. Sung, R.R. Dasari, M.W. Kirschner, C.J. Tabin, Multiple phases of chondrocyte enlargement underlie differences in skeletal proportions, Nature 495 (2013) 375–378.
[64] C.A. Poole, M.H. Flint, B.W. Beaumont, Chondrons in cartilage: ultrastructural analysis of the pericellular microenvironment in adult human articular cartilages, J. Orthop. Res. 5 (1987) 509–522.
[65] C. Wang, B.K. Brisson, M. Terajima, Q. Li, K. Hoxha, B. Han, A.M. Goldberg, X.S. Liu, M.S. Marcolongo, M. Enomoto-Iwamoto, M. Yamauchi, S.W. Volk, L. Han, Type III collagen is a key regulator of the collagen fibrillar structure and biomechanics of articular cartilage and meniscus, Matrix Biol 85-86 (2020) 47–67.
[66] S.S. Shapiro, M.B. Wilk, An analysis of variance test for normality (complete samples), Biometrika 52 (1965) 591–611.
[67] M.S. Bartlett, Properties of sufficiency and statistical tests, Proc. R. Soc. Lond. A 160 (1937) 268–282.
[68] B.L. Welch, On the comparision of several mean values: an alternative approach, Biometrika 38 (1951) 330–336.
[69] P.A. Games, J.F. Howell, Pairwise multiple comparison procedures with unequal N's and/or variances: a Monte Carlo study, J. Educ. Stat. 1 (1976) 113–125.
[70] D. Bates, M. Mächler, B. Bolker, S. Walker, Fitting linear mixed-effects models using lme4, J. Stat. Softw. 67 (1) (2015) 1–48.
[71] S. Holm, A simple sequentially rejective multiple test procedure, Scand. J. Statist. 6 (1979) 65–70.

[72] A. Acuna, M.A. Drakopoulos, Y. Leng, C.J. Goergen, S. Calve, Three-dimensional visualization of extracellular matrix networks during murine development, Dev. Biol. 435 (2018) 122–129.
[73] E.H. Morrison, M.W. Ferguson, M.T. Bayliss, C.W. Archer, The development of articular cartilage: I. The spatial and temporal patterns of collagen types, J. Anat. 189 (1996) 9–22.
[74] L. Ng, A.J. Grodzinsky, P. Patwari, J. Sandy, A. Plaas, C. Ortiz, Individual cartilage aggrecan macromolecules and their constituent glycosaminoglycans visualized via atomic force microscopy, J. Struct. Biol. 143 (2003) 242–257.
[75] J.E. Marturano, J.D. Arena, Z.A. Schiller, I. Georgakoudi, C.K. Kuo, Characterization of mechanical and biochemical properties of developing embryonic tendon, Proc. Natl. Acad. Sci. U. S. A. 110 (2013) 6370–6375.
[76] A.K. Williamson, A.C. Chen, R.L. Sah, Compressive properties and function-composition relationships of developing bovine articular cartilage, J. Orthop. Res. 19 (2001) 1113–1121.
[77] C. Canal Guterl, C.T. Hung, G.A. Ateshian, Electrostatic and non-electrostatic contributions of proteoglycans to the compressive equilibrium modulus of bovine articular cartilage, J. Biomech. 43 (2010) 1343–1350.
[78] D. Dean, L. Han, A.J. Grodzinsky, C. Ortiz, Compressive nanomechanics of opposing aggrecan macromolecules, J. Biomech. 39 (2006) 2555–2565.
[79] M.D. Buschmann, A.J. Grodzinsky, A molecular model of proteoglycan-associated electrostatic forces in cartilage mechanics, J. Biomech. Eng. 117 (1995) 179–192.
[80] D. Dean, J. Seog, C. Ortiz, A.J. Grodzinsky, Molecular-level theoretical model for electrostatic interactions within polyelectrolyte brushes: applications to charged glycosaminoglycans, Langmuir 19 (2003) 5526–5539.
[81] D. Heinegård, Proteoglycans and more – from molecules to biology, Int. J. Exp. Pathol. 90 (2009) 575–586.
[82] C. Baldock, M.J. Sherratt, C.A. Shuttleworth, C.M. Kielty, The supramolecular organization of collagen VI microfibrils, J. Mol. Biol. 330 (2003) 297–307.
[83] R.S. Decker, H.B. Um, N.A. Dyment, N. Cottingham, Y. Usami, M. Enomoto-Iwamoto, M.S. Kronenberg, P. Maye, D.W. Rowe, E. Koyama, M. Pacifici, Cell origin, volume and arrangement are drivers of articular cartilage formation, morphogenesis and response to injury in mouse limbs, Dev. Biol. 426 (2017) 56–68.
[84] R.S. Decker, E. Koyama, M. Pacifici, Articular cartilage: structural and developmental intricacies and questions, Curr. Osteoporos. Rep. 13 (2015) 407–414.
[85] F. Jenner, I.J. A, M. Cleary, D. Heijsman, R. Narcisi, P.J. van der Spek, A. Kremer, R. van Weeren, P. Brama, G.J. van Osch, Differential gene expression of the intermediate and outer interzone layers of developing articular cartilage in murine embryos, Stem Cells Dev 23 (2014) 1883–1898.
[86] M. Pacifici, M. Iwamoto, E.B. Golden, J.L. Leatherman, Y.S. Lee, C.M. Chuong, Tenascin is associated with articular cartilage development, Dev. Dyn. 198 (1993) 123–134.
[87] S. Bhumiratana, R.E. Eton, S.R. Oungoulian, L.Q. Wan, G.A. Ateshian, G. Vunjak-Novakovic, Large, stratified, and mechanically functional human cartilage grown *in vitro* by mesenchymal condensation, Proc. Natl. Acad. Sci. U.S.A. 111 (2014) 6940–6945.
[88] Y. Sun, L. Yan, S. Chen, M. Pei, Functionality of decellularized matrix in cartilage regeneration: a comparison of tissue versus cell sources, Acta Biomater. 74 (2018) 56–73.
[89] X. Wang, Y. Lu, W. Wang, Q. Wang, J. Liang, Y. Fan, X. Zhang, Effect of different aged cartilage ECM on chondrogenesis of BMSCs in vitro and in vivo, Regen. Biomater. 7 (2020) 583–595.
[90] B. Doyran, W. Tong, Q. Li, H. Jia, X. Zhang, C. Chen, M. Enomoto-Iwamoto, X.L. Lu, L. Qin, L. Han, Nanoindentation modulus of murine cartilage: a sensitive indicator of the initiation and progression of post-traumatic osteoarthritis, Osteoarthritis Cartilage 25 (2017) 108–117.
[91] T. Wang, J.H. Lai, F. Yang, Effects of hydrogel stiffness and extracellular compositions on modulating cartilage regeneration by mixed populations of stem cells and chondrocytes in vivo, Tissue Eng. Part A 22 (2016) 1348–1356.
[92] D.E. Pazin, L.W. Gamer, L.P. Capelo, K.A. Cox, V. Rosen, Gene signature of the embryonic meniscus, J. Orthop. Res. 32 (2014) 46–53.
[93] T.K. Tsinman, X. Jiang, L. Han, E. Koyama, R.L. Mauck, N.A. Dyment, Intrinsic and growth-mediated cell and matrix specialization during murine meniscus tissue assembly, FASEB J 35 (2021) e21779.
[94] J. Melrose, S. Smith, M. Cake, R. Read, J. Whitelock, Comparative spatial and temporal localisation of perlecan, aggrecan and type I, II and IV collagen in the ovine meniscus: an ageing study, Histochem. Cell Biol. 124 (2005) 225–235.
[95] R. Sadatsuki, H. Kaneko, M. Kinoshita, I. Futami, R. Nonaka, K.L. Culley, M. Otero, S. Hada, M.B. Goldring, Y. Yamada, K. Kaneko, E. Arikawa-Hirasawa, M. Ishijima, Perlecan is required for the chondrogenic differentiation of synovial mesenchymal cells through regulation of Sox9 gene expression, J. Orthop. Res. 35 (2017) 837–846.
[96] T.L. Vincent, C.J. McLean, L.E. Full, D. Peston, J. Saklatvala, FGF-2 is bound to perlecan in the pericellular matrix of articular cartilage, where it acts as a chondrocyte mechanotransducer, Osteoarthritis Cartilage 15 (2007) 752–763.
[97] W.M. Han, S.J. Heo, T.P. Driscoll, J.F. Delucca, C.M. McLeod, L.J. Smith, R.L. Duncan, R.L. Mauck, D.M. Elliott, Microstructural heterogeneity directs micromechanics and mechanobiology in native and engineered fibrocartilage, Nat. Mater. 15 (2016) 477–484.
[98] Q. Li, B. Doyran, L.W. Gamer, X.L. Lu, L. Qin, C. Ortiz, A.J. Grodzinsky, V. Rosen, L. Han, Biomechanical properties of murine meniscus surface via AFM-based nanoindentation, J. Biomech. 48 (2015) 1364–1370.